EMV-Untersuchungen für die Qualifizierung von elektrischen Orbitalantrieben für Satelliten

Dissertation

zur Erlangung des akademischen Grades

Doktor der Ingenieurwissenschaften

(Dr.-Ing.)

vorgelegt dem

Promotionszentrum für Ingenieurwissenschaften

des Forschungscampus Mittelhessen

von

Yannik Rover, M.Sc. MBA Eng.

aus Marburg

Gießen, Januar 2024

Diese Arbeit wurde zur Erlangung des akademischen Grades eines Doktors der Ingenieurwissenschaften dem Promotionszentrum für Ingenieurwissenschaften des Forschungscampus Mittelhessen vorgelegt.

Einreichung: 31.01.2024
Disputation:

Betreuer Justus-Liebig-Universität:	Prof. Dr.-Ing. Uwe Probst
Betreuer Technische Hochschule Mittelhessen:	Prof. Dr. rer. nat. Chris Volkmar

Eidesstattliche Erklärung

Ich erkläre: Ich habe die vorgelegte Dissertation selbstständig und ohne unerlaubte fremde Hilfe und nur mit den Hilfen angefertigt, die ich in der Dissertation angegeben habe. Alle Textstellen, die wörtlich oder sinngemäß aus veröffentlichten Schriften entnommen sind, und alle Angaben, die auf mündlichen Auskünften beruhen, sind als solche kenntlich gemacht. Ich stimme einer evtl. Überprüfung meiner Dissertation durch eine Antiplagiat-Software zu. Bei den von mir durchgeführten und in der Dissertation erwähnten Untersuchungen habe ich die Grundsätze guter wissenschaftlicher Praxis, wie sie in der entsprechenden Satzung der federführenden Hochschule niedergelegt sind und die mir ausgehändigt wurde, eingehalten.

Amöneburg, den 31.01.2024

Yannik Rover

Abstract

This thesis is a cumulative dissertation. The research work focusses on investigations of the electromagnetic compatibility (EMC) of orbital propulsion systems for satellites. The basis of this work is the advancing commercial use of electric propulsion (EP) systems. A radio-frequency ion thruster (RIT) is available for this purpose as a representative for electrostatic thrusters. Publications in subject-specific journals document the work carried out and show the knowledge gained. This involves the generation and expansion of simulation models for the thruster, its ion beam and peripheral components. Furthermore, the construction and commissioning of a semi-anechoic chamber (SAC) with a vacuum tank is described. This paper serves to classify and summarize the published contributions, which have created a comprehensive understanding of the subject areas and in turn made new work possible. The influences on the EMC of a thruster caused by a radio-frequency generator and an ion beam can be predicted by simulations and will be combined in further steps to obtain a comprehensive model. The optimized semi-anechoic chamber eliminates the weaknesses of existing, comparable test facilities and enables meaningful analyses.

Kurzzusammenfassung

Bei dieser Arbeit handelt es sich um eine kumulative Dissertation. Die Forschungsarbeit beschäftigt sich mit Untersuchungen der elektromagnetischen Verträglichkeit (EMV) an Orbitalantrieben für Satelliten. Grundlage dieser Arbeit ist die voranschreitende kommerzielle Nutzung von elektrischen Raumfahrtantrieben. Hierfür steht ein Radiofrequenz-Ionentriebwerk (RIT) als Stellvertreter der elektrostatischen Triebwerke zur Verfügung. Veröffentlichungen in themenspezifischen Journalen dokumentieren die durchgeführten Arbeiten und zeigen die gewonnenen Erkenntnisse. Dabei handelt es sich um die Generierung und Erweiterung von Simulationsmodellen für das Triebwerk, inklusive Ionenstrahl, wie auch dessen Peripheriekomponenten. Weiterhin sind der Aufbau und die Inbetriebnahme einer halb-reflexionsfreien Absorberkammer mit Vakuumtank beschrieben. Diese Ausarbeitung dient der Einordnung und Zusammenfassung der veröffentlichten Beiträge, durch welche ein umfassendes Wissen innerhalb der Themenfelder entstanden ist und somit wiederum neue Arbeiten ermöglicht werden. Die Einflüsse auf die EMV eines Triebwerks, durch einen Radiofrequenz-Generator sowie einen Ionenstrahl, sind durch Simulationen nun vorhersagbar und werden in weiteren Schritten zusammengeführt,

um ein umfassendes Modell zu erhalten. Die optimierte halb-reflexionsfreie Absorberkammer eliminiert die Schwächen bestehender, vergleichbarer Testeinrichtungen und ermöglicht aussagekräftige Analysen.

Danksagung

An dieser Stelle möchte ich mich bei allen Menschen bedanken, die mich während meiner Tätigkeit als wissenschaftlicher Mitarbeiter unterstützt haben. Zunächst möchte ich besonderen Dank meinem Betreuer seitens der Technischen Hochschule Mittelhessen Prof. Dr. rer. nat. Chris Volkmar aussprechen, der mich während der Promotion förderte und insbesondere für das Themengebiet der elektromagnetischen Verträglichkeit begeistern konnte. Seine fachliche Expertise und die konstruktiven Gespräche halfen mir diese Arbeit erfolgreich zu bewältigen. Dabei hatte er stets ein offenes Ohr für Fragen und motivierte mich. Ich möchte seine freundliche Art und die engagierte Betreuung betonen, die eine tolle Zusammenarbeit in der Arbeitsgruppe erst ermöglichten. In gleichem Maße möchte ich mich bei meinem Betreuer Prof. Dr.-Ing. Uwe Probst bedanken, der mir mit seiner Erfahrung und den hilfreichen Ratschlägen jederzeit zur Seite stand und mich durchgängig unterstützte. Seine positive und offene Art vermittelten Zuversicht bei der Problemlösung. Unsere Gespräche waren durchweg sehr bereichernd und haben mich motiviert, die Promotion zielstrebig durchzuführen. Weiterhin möchte ich mich bei den ehemaligen und aktuellen Mitgliedern der Arbeitsgruppe Raumfahrtelektronik Prof. Dr. rer.

nat. Rainer Thüringer, Prof. Dr. rer. nat. Jens Simon, Dr. rer. nat. Timo Baruth, Dr. rer. nat. Andreas Reeh, Dr.-Ing. Jan Erik Junker, Christian Rößler, Tobias Sommavilla, Edwin Beller, Philip Peters, Erik Jozsef und Luca Henrich für die tolle Zusammenarbeit bedanken. Das Arbeitsklima innerhalb der Gruppe war stets angenehm. Weiterer Dank gilt meinem Kollegen Malte Nickel, der mich während der Promotion ebenfalls tatkräftig unterstützte und jederzeit für positive Stimmung sorgte. Des Weiteren danke ich den Mitgliedern der AG Ionentriebwerke der Justus-Liebig-Universität, die sehr aufgeschlossen und hilfsbereit waren den gemeinsamen Forschungsschwerpunkt voranzutreiben. Besonderer Dank gilt hier der Leitung um Prof. Dr. Peter J. Klar sowie Dr. Kristof Holste. Die Kollegen Felix Kiefer und Konstantin Keil haben mich während der experimentellen Untersuchungen mit großem Einsatz unterstützt. Nicht zuletzt gilt meiner Familie und meinen Freunden besonderer Dank für die umfassende Unterstützung und den notwendigen Rückhalt in dieser Zeit. Die vorliegende Arbeit wurde im Rahmen eines Drittmittelprojektes „EMV-Untersuchungen für die Qualifizierung von elektrischen Orbitalantrieben für Satelliten“ durch das Bundesministerium für Bildung und Forschung (BMBF) unter dem Kennzeichen 13FH173PX8 gefördert.

Veröffentlichungen und Konferenzbeiträge

- Rover, Y., Volkmar, C.: “Verification of a radio-frequency generator model in a full-wave 3D EM simulation”, 2022 IEEE Aerospace Conference (AERO), Big Sky, MT, USA, 2022, pp. 1-10, https://doi.org/10.1109/ AERO53065.2022.9843355 **(Beitrag zu dieser Dissertation)**
- Rover, Y., Thüringer, R., Volkmar, C., Probst, U., Kiefer, F., Holste, K., Klar, P. J.: “Semi-anechoic chamber for EMC tests of EP thrusters”, IEPC-2022-240, 2022 International Electric Propulsion Conference, Massachusetts Institute of Technology, Cambridge, MA, USA, 2022, https://www.electricrocket.org/IEPC_2022_Papers.html
- Kiefer, F., Holste, K., Klar, P. J., Rover, Y., Probst, U., Volkmar, C.: “Reverberation chamber for electromagnetic compatibility testing of electric thrusters”, IEPC-2022-257, 2022 International Electric Propulsion Conference, Massachusetts Institute of Technology, Cambridge, MA, USA, 2022, https://www.electricrocket.org/IEPC_2022_Papers.html

- Rover, Y., Thüringer, R., Volkmar, C., Probst, U., Kiefer, F., Holste, K., Klar, P. J.: "Semi-anechoic chamber for electromagnetic compatibility tests of electric propulsion thrusters", J Electr Propuls 2, 3 (2023), https://doi.org/10.1007/s44205-023-00039-w **(Beitrag zu dieser Dissertation)**
- Kiefer, F., Holste, K., Klar, P. J., Rover, Y., Probst, U., Volkmar, C.: "Reverberation chamber for electromagnetic compatibility testing of electric thrusters", J Electr Propuls 2, 9 (2023), https://doi.org/10.1007/s44205-023-00038-x
- Rover, Y., Thüringer, R., Probst, U., Volkmar, C.: "Modeling the influence of an electric thruster's ion beam on its global EMC", Front. Space Technol. 4:1287474 (2023), https://doi.org/10.3389/frspt.2023.1287474 **(Beitrag zu dieser Dissertation)**

Inhaltsverzeichnis

Abbildungsverzeichnis

Symbolverzeichnis

Symbol	Bedeutung	Einheit
$\vec{E}$	elektrisches Feld	V/m
$\vec{F}$	Kraft	N
$\vec{F}_\mathrm{T}$	Schubkraft	N
f	Frequenz	Hz
$\vec{H}$	magnetisches Feld	A/m
I, i	Strom	A
k	Wellenzahl	1/m
λ	Wellenlänge	m
m	Treibstoffmasse	kg
m_0	Startmasse	kg
m_e	Endmasse	kg
$\vec{p}$	Impuls	N s
r	Abstand zur Quelle	m
t	Zeit	s
U, u	Spannung	V

Symbol	Bedeutung	Einheit
Δv	Änderungsgeschwindigkeit	$\mathrm{m/s}$
v_{ex}	Austrittsgeschwindigkeit	$\mathrm{m/s}$
Z_0	Wellenwiderstand (Wellenimpedanz) freier Raum	Ω
Z_{c}	Wellenwiderstand (Wellenimpedanz)	Ω

Naturkonstanten

Symbol	Bedeutung	Größe
c_0	Lichtgeschwindigkeit	$299\,792\,458\ \mathrm{m/s}$
ϵ_0	Dielektrizitätskonstante	$8,854 \cdot 10^{-12}\ \mathrm{As/Vm}$
μ_0	magnetische Feldkonstante	$4\,\pi \cdot 10^{-7}\ \mathrm{Vs/Am}$
π	Kreiszahl	$3,141592$

Abkürzungsverzeichnis

CM	Common Mode, deutsch: Gleichtaktmode
DC	Direct current, deutsch: Gleichstrom
DM	Differential Mode, deutsch: Gegentaktmode
EMC	Electromagnetic Compatibility, deutsch: Elektromagnetische Verträglichkeit
EMV	Elektromagnetische Verträglichkeit
EP	Electric Propulsion, deutsch: Elektrische Raumfahrtantriebe
ESA	European Space Agency, deutsch: Europäische Weltraumorganisation
GTEM	Gigahertz Transversal Elektromagnetisch
HF	Hochfrequenz
IEEE	Institute of Electrical and Electronics Engineers
IEPC	International Electric Propulsion Conference
kHz	Kilohertz
MHz	Megahertz
RF	Radiofrequenz

RFG	Radiofrequenz-Generator
RIM	Radiofrequenz-Ionenquelle für Materialbearbeitung
RIT	Radiofrequenz-Ionentriebwerk
SAC	semi-anechoic chamber, deutsch: halb-reflexionsfreie Absorberkammer
Xe	Xenon

1 Einleitung

Diese Arbeit beschäftigt sich mit EMV-Untersuchungen für die Qualifizierung von elektrischen Orbitalantrieben für Satelliten. Heutzutage sind elektrische Triebwerke wichtige Antriebssysteme im Weltraum. Die zunehmende Kommerzialisierung hat einen großen Einfluss auf die Raumfahrt und insbesondere auf elektrische Antriebe. Wesentliche Motive für die aufkommende Raumfahrt sind wissenschaftliche, politische, militärische und wirtschaftliche Ziele. Die noch bestehenden Herausforderungen führen zu umfangreichen Forschungen in den Bereichen Energieeffizienz, elektromagnetische Verträglichkeit, alternative Treibstoffe, Skalierbarkeit und weiteren Gebieten [**Hol20**].

Diese kumulative Dissertation beschäftigt sich mit der elektromagnetischen Verträglichkeit im Anwendungsgebiet der Raumfahrt, speziell der elektrischen Triebwerke sowie deren peripheren Komponenten. Ziel dieser Forschungsarbeit ist die Bearbeitung und Forcierung einzelner Schwerpunktthemen wie Simulationsmodellen sowie der Aufbau einer Testeinrichtung. Dazu werden vereinzelt vorangegangene Arbeiten aufgegriffen und weiterentwickelt. Baruth [**Bat17**] erstellte und analysierte ein Simulationsmodell des RIM-4 (Abwandlung

eines RIT-4 zur Materialbearbeitung). Hierauf gilt es nun aufzubauen und dem Modell weitere Komponenten eines elektrischen Antriebssystems hinzuzufügen. Zudem ist die Errichtung und Inbetriebnahme einer EMV-Testeinrichtung vorgesehen. Dadurch ist es möglich, ein Triebwerk unter realen Betriebsbedingungen zu verwenden und aus EMV-Sicht zu vermessen. Diverse Aufbauten, Konfigurationen und Parameter des Triebwerkssystems werden analysiert und gegenübergestellt. Die Gliederung dieser Arbeit ist daher wie folgt: Kapitel 1.1 zeigt zu Beginn die Motivation auf, woraufhin der Stand der Wissenschaft (Kap. 1.2) folgt. Weiterhin sind die wissenschaftliche Fragestellung dieser Promotion und die daran anknüpfende Zielsetzung in Kap. 1.3 gegeben. Anschließend wird ein Überblick über die wichtigsten Grundlagen dieser Arbeit (Kap. 2) aufgezeigt. Die veröffentlichten Beiträge zu dieser Arbeit werden in Kap. 3 vorgestellt und in die Gesamtthematik eingeordnet. Abschließend führt Kap. 4 eine Diskussion über die Forschungsarbeit.

1.1 Motivation

Aufgrund des zunehmenden Einsatzes von elektrischen Triebwerken sowie der hohen Dichte an elektronischen Systemen auf einem Satelliten, die von der Kommunikationselektronik bis zur Elektronik des Antriebssystems reichen, gewinnen Aspekte der EMV zunehmend an Bedeutung. Neben den etablierten Systemen, die ihre Verträglichkeit durch erfolgreichen Einsatz sicher bewiesen haben, betreffen EMV-Aspekte die neuartigen EP-Konzepte. Etablierte Syste-

me haben einen abgeschlossenen Entwicklungsstand und bereits erfolgreiche Weltraumeinsätze absolviert.

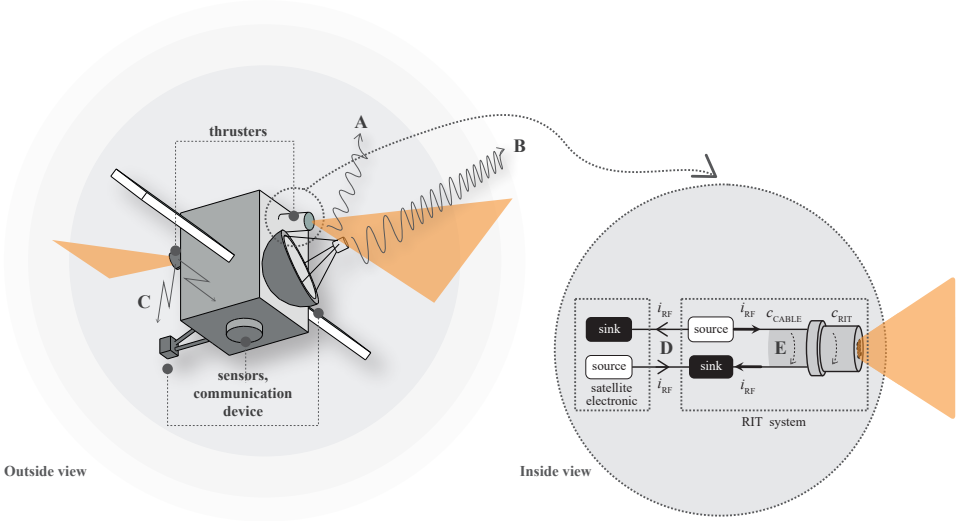

Abbildung 1.1: Interaktionen zwischen Triebwerkssystem, inklusive Versorgungselektronik, („RIT system“) und Satellitenelektronik („satellite electronic“), (Abb. 17a in [**Hol20**]).

Wie Abb. 1.1 zeigt, existieren diverse Kopplungsmechanismen zwischen den Systemen auf einem Satelliten. Diese Störungen gilt es zu identifizieren und auf ein betriebssicheres Niveau zu limitieren:

- A: Abgestrahlte Emissionen des Ionenstrahls
- B: Beeinflussung von Kommunikationssignalen durch den Ionenstrahl
- C: Elektromagnetische Felder und Emissionsstrahlung des Triebwerks
- D: Leitungsgebundene Störungen zwischen den Satellitensystemen
- E: EMV-Interaktionen innerhalb des Triebwerkssystems: gegenseitige Beeinflussung der Komponenten

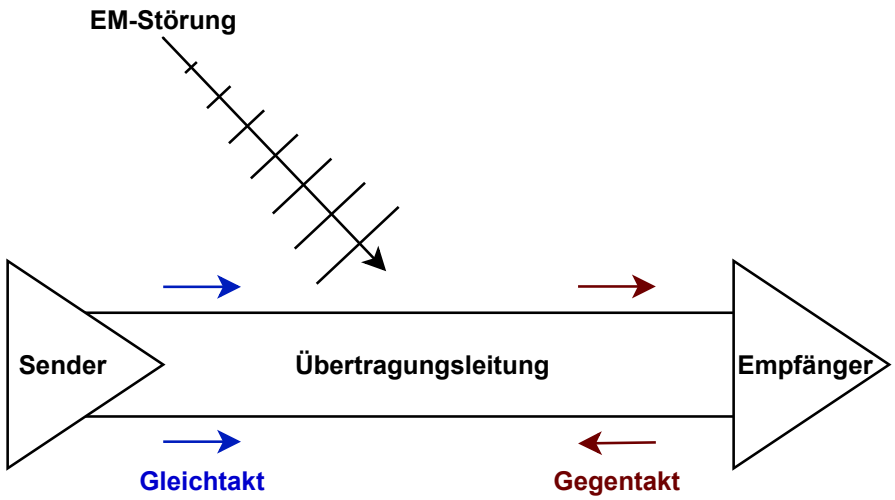

Abbildung 1.2: Gleichtakt- und Gegentaktstörung in einem Schaltkreis, hervorgerufen durch eine externe elektromagnetische Störung.

Beispielsweise können HF-Leitungsströme fehlerhafte Sensormessungen verursachen, da deren elektromagnetische Felder über Kopplungspfade für leitungsgebundene Störpotentiale und Abstrahlungen sorgen. Grundlage davon sind zwei mögliche Ausbreitungsmoden, der Gleichtakt- und Gegentaktbetrieb, siehe zur Verdeutlichung Abb. 1.2. Der Gegentaktmode (engl. Differential Mode, DM) zeichnet sich durch einen betraglich gleich großen Strom mit entgegengesetztem Vorzeichen aus. Beim Gleichtaktmode (engl. Common Mode, CM) hingegen haben die Ströme die gleichen Beträge und Vorzeichen. Die verursachten Nahfelder der gegensinnigen DM-Ströme kompensieren sich, die der CM-Ströme superponieren. Bei gleicher HF-Stromstärke sind die Felder des Gleichtaktmode demnach deutlich stärker als die des Gegentaktmode und haben aus EMV-Sicht eine größere Bedeutung.

Alle Systemkomponenten eines EP-Systems sowie sämtliche Betriebsarten können in einer umfassenden EMV-Analyse berücksichtigt werden. Um rasche und damit kostengünstige Entwicklungszyklen zu ermöglichen, ist es erstrebenswert, bereits in den frühen Entwicklungsstadien elektrischer Komponenten für EP-Systeme auf EMV-Untersuchungen zurückzugreifen. Der Aufwand und damit die Kosten, EMV-sichernde Maßnahmen durchzuführen, steigen mit dem Fortschritt im Entwicklungszyklus. EMV-Fragen, die die elektromagnetische Wechselwirkung zwischen den Komponenten von Satellitensystemen betreffen, sind für alle Missionen von großer Bedeutung. Um eine einwandfreie und zuverlässige Funktion sowohl des Triebwerks als auch der Komponenten des Satellitensystems sicherzustellen, ist es notwendig, die potenziellen elektromagnetischen Wechselwirkungen (Kopplungsmechanismen) zu identifizieren und die Stärke der HF-Störströme sowie der emittierten elektromagnetischen Felder zu begrenzen. Die Untersuchungen der Wechselwirkungen werden in der Regel mit Hilfe von 3D-Simulationsmodellen durchgeführt. Die Elektronikbaugruppen stellen etwa 60 % aller Baugruppen eines Triebwerkssystems dar, was zeigt, wie wichtig es ist, diese vermeintlich peripheren Komponenten und ihre Wechselwirkung mit dem Triebwerk und anderen Satellitenkomponenten zu untersuchen [**Hol20**].

1.2 Stand der Wissenschaft

Der Stand der Wissenschaft knüpft direkt an die Motivation an. Bisherige Verfahren zur Sicherstellung der elektromagnetischen Verträglichkeit prüfen lediglich

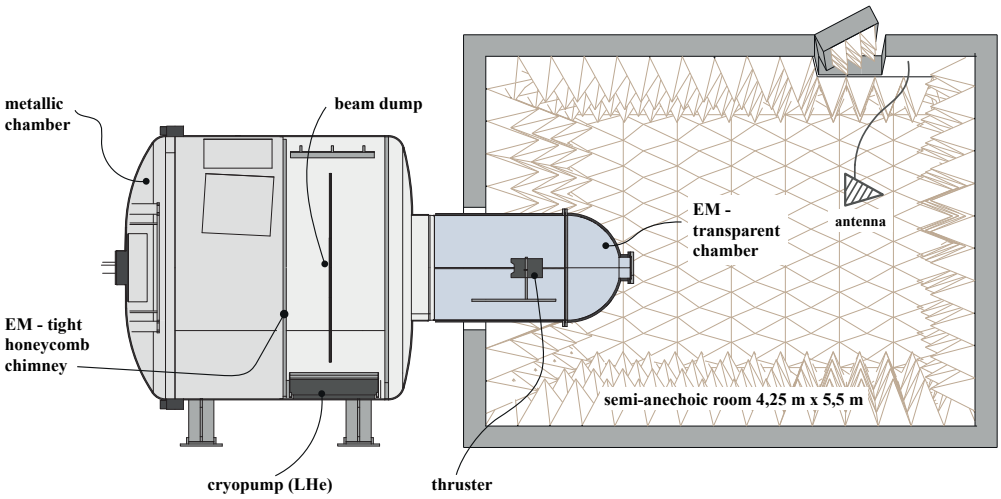

Abbildung 1.3: Schematische Skizze der halb-reflexionsfreien Testeinrichtung an der Justus-Liebig-Universität Gießen, (Abb. 18c in [**Hol20**]).

Teilkomponenten, entweder durch Simulation oder messtechnische Untersuchungen. Dabei handelt es sich um einzelne Bereiche der komponenteninternen Elektronik, wie beispielsweise eine Platine. Diese Analysen beziehen weder alle Funktionen einer Komponente ein, noch betrachten sie die Baugruppe ganzheitlich. Weiterhin werden die Besonderheiten der Raumfahrt nicht berücksichtigt, siehe dazu Kap. 2. Die EMV-Qualifizierung eines elektrischen Antriebssystems inklusive der Energieversorgung und Regelung erfolgt oft erst im Rahmen des abschließenden Qualifikationsprogramms. Häufig werden dann Inkompatibilitäten zwischen Anforderungen und tatsächlichem Verhalten festgestellt. In diesem Stadium ist dann lediglich eine Behebung der Problemstellungen möglich, nicht jedoch die Erforschung und Beseitigung des Ursprungs.

Dem Autor sind keine Simulationsmodelle bekannt, welche speziell die Komponenten eines elektrischen Triebwerks abbilden und analysieren. Baruth [**Bat17**] entwickelte und analysierte ein RIM-4 Simulationsmodell, das in dieser Arbeit verwendet wird. Die derzeit genutzten EMV-Analysen und Vorhersagen während der Entwicklung, noch vor der Produktion und des Betriebs, bieten großes Verbesserungspotenzial für die entwickelten Komponenten. Weiterhin existieren lediglich wenige Einrichtungen weltweit, um die Triebwerkssysteme ganzheitlich hinsichtlich EMV-Aspekten zu analysieren. Müller, Kukies und Bassner [**Mue92**] führten die ersten Vermessungen durch. Dabei befindet sich das RIT in einem Vakuumzylinder aus Glas, Antennen erfassen das Emissionsspektrum in einem bestimmten Frequenzbereich von außen. Die gleichzeitige Erfassung von Umgebungsstörsignalen beeinträchtigt die Messergebnisse und kann sie verändern. Weiterhin sind aufgrund des Glaszylinders und der inneren Ablagerungen durch den Extraktionsbetrieb die Messwerte nur bedingt aussagekräftig und können leicht verfälscht werden. Eine Kombination aus Absorberraum und Vakuumtank bietet die Möglichkeit, das Triebwerk während des Betriebs ohne Hintergrundstörungen zu analysieren. Anlagen, die ein solches Prinzip umsetzen, werden in [**Bar17**; **Bei03**; **Men16**; **Zha21**] beschrieben. Bei den Ausführungen der Einrichtungen handelt es sich um halb-reflexionsfreie (engl. semi-anechoic) Anlagen. Hierbei ist die eigentliche Absorberkammer weitestgehend durch entsprechende Absorber gegen Reflexionen geschützt. Die metallischen Wände schützen vor Einkopplungen. Dieser Schutz trifft nicht auf die Verbindung von Absorberkammer und Vakuumtank zu: Der Übergang sowie die Flanschöffnungen am Vakuumtank, für Messeinrichtungen und Pumpen, sind ein Einfallstor für externe elektromagnetische Störungen und werden

in dieser Arbeit thematisiert. Eine schematische Darstellung der Testeinrichtung an der Justus-Liebig-Universität Gießen ist in Abb. 1.3 dargestellt und wird in dieser Arbeit beschrieben.

1.3 Wissenschaftliche Fragestellung und Zielsetzung

Aufbauend auf dem Stand der Wissenschaft lässt sich für die folgenden Themen ein Forschungsbedarf ableiten:

- Simulationsmodelle, welche ganzheitlich eine Baugruppe bestehend aus Triebwerk und versorgender Elektronik analysieren, existieren bislang nicht. Selbst die einzelnen Komponenten der versorgenden Elektronik sind bisher nicht simulationstechnisch untersucht. Aus diesem Grund ist ein umfassendes Simulationsmodell des Radiofrequenz-Generators erstellt und messtechnisch verifiziert worden. Die erste Veröffentlichung greift die erstellte RFG-Simulation auf und befasst sich mit der messtechnischen Verifikation des Modells [**Rov22**].
- Eine weitere Fragestellung betrifft die Wechselwirkung des Ionenstrahls mit dem, ihn erzeugenden, Triebwerkssystem. Die zweite Veröffentlichung erläutert das zugehörige Simulationsmodell und zeigt dabei das Vorgehen und die adaptierbaren Parameter des Konstrukts, um den Ionenstrahl abzubilden [**Rov23**].
- Bei den erwähnten Testeinrichtungen aus [**Bar17**; **Bei03**; **Men16**; **Zha21**] handelt es sich um halb-reflexionsfreie Absorberkammern. Durch die bau-

artbedingten Einschränkungen entstehen Nachteile und Unsicherheiten, welche sich negativ auf die Triebwerks-Untersuchungen auswirken. Dies beruht zum einen auf der fehlenden Schirmung an der Verbindungsstelle von Absorberraum und Vakuumtank, wodurch externe elektromagnetische Störungen eindringen können. Des Weiteren gelangen Störsignale durch Anbauteile des Vakuumtanks in das Messgebiet. Aus diesem Grund ist am I. Physikalischen Institut der Justus-Liebig-Universität in Gießen eine optimierte halb-reflexionsfreie Testeinrichtung entstanden, um die bekannten Schwächen zu eliminieren. Die dritte Veröffentlichung bezieht sich auf deren Konstruktion sowie die ersten Untersuchungen an elektrischen Triebwerken [**Roy23**].

Die Ergebnisse dieser Arbeit erweitern in vielerlei Hinsicht den Stand der Wissenschaft und zeigen dabei neue Möglichkeiten der Analyse zu EMV-Eigenschaften der gesamten Triebwerksbaugruppe auf.

- Das Verhalten von einzelnen entscheidenden Komponenten ist durch Simulationen nun vorhersagbar.
- Die optimierte halb-reflexionsfreie Absorberkammer eliminiert die Schwächen bestehender, vergleichbarer Testeinrichtungen und ermöglicht auf Forschungs- sowie kommerzieller Ebene aussagekräftige Analysen.
- Die Vorteile einer Kombination von Simulation und Messung sind nutzbar.

Speziell bei Messverfahren mit diversen Aufbauten und Messkomponenten für bestimmte Bereiche (elektrische Größen, Frequenzspektren), ist es oft sinnvoll ein Simulationsmodell zu nutzen, sofern das Vorgehen experimentell validiert

ist. In Langzeitmessungen oder bei der Untersuchung von Alterungsprozessen mit anschließender Überprüfung des Systemverhaltens kann eine Simulation oft zu schnelleren Ergebnissen führen. Messungen hingegen können effizienter sein, wenn Erwartungswerte bekannt sind und der Aufwand gering ist. Das trifft auch zu, wenn es um unbekannte Systeme geht, für die noch kein Simulationsmodell existiert. Die (Teil-)Ergebnisse von Simulation oder Messung sind ebenfalls nützlich, um sie bei der jeweils anderen Methode einzusetzen. Beispielsweise lässt sich das gemessene Emissionsspektrum einer Komponente als Störquelle im Simulationsprogramm verwenden, um weiterführende Simulationen oder gegenseitige Beeinflussungen zu prüfen. Im Falle eines unbekannten Systemverhaltens ist es möglich, erste Ergebnisse durch eine Simulation zu erhalten, ehe die Messung durchgeführt wird. Durch eine physikalische Plausibilitätsprüfung und die Simulation wird bekannt, welche Größen zu erwarten sind und welches Messequipment nötig ist.

2 Überblick der Themengebiete

Um Satelliten und weitere Raumfahrzeuge translatorisch zu bewegen, werden Triebwerke benötigt. Die Fortbewegung basiert auf dem physikalischen Prinzip der Impulserhaltung, bei der der Treibstoff entgegen der Bewegungsrichtung ausgestoßen wird. Die zeitliche Änderung eines Impulses entspricht der wirkenden Kraft nach Gleichung (2.1):

$$F = \frac{\mathrm{d}p}{\mathrm{d}t} \tag{2.1}$$

Mit dem Impuls p aus Gleichung (2.2)

$$p = m \cdot v, \tag{2.2}$$

folgt

$$F = \frac{\mathrm{d}p}{\mathrm{d}t} = \frac{\mathrm{d}m}{\mathrm{d}t} \cdot v + m \cdot \frac{\mathrm{d}v}{\mathrm{d}t}. \tag{2.3}$$

Unter der Annahme einer konstanten Geschwindigkeit v ergibt sich die Schubkraft F_T durch Gleichung (2.4):

$$F_\mathrm{T} = \frac{\mathrm{d}m}{\mathrm{d}t} \cdot v_\mathrm{ex} = \dot{m} \cdot v_\mathrm{ex} \tag{2.4}$$

Die Schubkraft wird demnach größer, wenn mehr Treibstoffmasse m pro Zeit t und mit einer höheren Geschwindigkeit v_ex ausgestoßen wird. Die Raketengleichung von Konstantin Ziolkowski lässt sich durch den Impulserhaltungssatz sowie weiterer Annahmen, wie einer konstanten Austrittsgeschwindigkeit, herleiten (Gleichung (2.5)) [**Cha11**]:

$$\Delta v = v_\mathrm{ex} \cdot \ln\left(\frac{m_0}{m_\mathrm{e}}\right) \tag{2.5}$$

Während des Schubbetriebs ändert sich die Masse des Raumfahrzeugs von m_0 beim Zünden zu m_e beim Brennschluss der Triebwerke. Gleichung (2.5) beschreibt, dass die Geschwindigkeitsänderung des Raumfahrzeugs direkt von der Austrittsgeschwindigkeit des Treibstoffs abhängt. Bei chemischen Triebwerken wird die Masse erhitzt, in Wärmeenergie gewandelt und über eine Düse ausgestoßen. Durch die Energie der chemischen Bindungen ist die Austrittsgeschwindigkeit der Masse limitiert. Bei elektrischen Triebwerken wiederum ist die Extraktion in erster Näherung lediglich durch die zur Verfügung stehende elektrische Energie eingeschränkt [**Cha11**].

Im Falle der elektrischen Triebwerke gibt es drei physikalische Prinzipien zur Schuberzeugung [**Hol20**]:

- Elektrothermische Triebwerke erhitzen den Treibstoff elektrisch. Schub wird durch thermodynamische Ausdehnung des Gases erzeugt.
- Elektrostatische Triebwerke beschleunigen die geladenen Ionen durch ein elektrostatisches Feld, um einen Schub zu generieren. Die zurückbleibenden Elektronen werden gesondert über Neutralisatoren aus dem Triebwerk geleitet. Das RIT ist ein Vertreter dieser Triebwerksgattung.
- Elektromagnetische Triebwerke nutzen eine elektromagnetische Beschleunigung (Lorentzkraft), um alle Teilchen des Plasmas gemeinsam zu extrahieren. Ausschließlich die Ionen tragen zur Schuberzeugung bei.

Wie alle elektrischen Triebwerke verwendet auch das Radiofrequenz-Ionentriebwerk elektrische Energie aus Sonnenkollektoren für seinen Betrieb. Die verfügbare Leistung ist jedoch aufgrund technologischer Einschränkungen wie Energiespeicherung oder der Effizienz der Leistungselektronik begrenzt. Aufgrund dieser Faktoren ist die Austrittsgeschwindigkeit der Ionen ebenfalls limitiert. Derzeit erreichen die ausgestoßenen Ionen eine Geschwindigkeit von 30 km/s bis 50 km/s. Das ist etwa zehnmal höher als die Ausstoßgeschwindigkeit von chemischen Triebwerken. Daher haben elektrische Triebwerke eine höhere Masseneffizienz - ein besseres Verhältnis von Schubkraft pro Treibstoffteilchen [**Hol20**]. Diesen positiven Eigenschaften stehen zwei Nachteile gegenüber: Erstens arbeiten Ionentriebwerke ausschließlich im Hochvakuum und nicht unter Atmosphärendruck, sodass ein Start von einem Planeten aus nicht möglich ist. Zweitens ist die Schubkraft dieser Triebwerke sehr gering und liegt aufgrund der begrenzten elektrischen Leistung im Bereich von Mikronewton bis etwa einem halben Newton. Daher entfalten sie ihre Vorteile im

Weltraum unter geringer Schwerkraft. Ein Beispiel hierfür ist das sogenannte „station-keeping“-Manöver, bei dem die Triebwerke Gravitationswirkungen ausgleichen und das Raumfahrzeug auf seiner Umlaufbahn stabilisieren.

Radiofrequenz-Generator

Der Radiofrequenz-Generator versorgt die Triebwerksspule mit Energie, steuert den Arbeitspunkt des Triebwerks und ist wesentlicher Bestandteil einer RIT-Baugruppe. Er liefert einen hochfrequenten, sinusförmigen Strom zur induktiven Einkopplung von elektrischer Energie in das Plasma. Der Frequenzbereich hängt unter anderem von der Geometrie des Ionisationsgefäßes und der Spule ab. Weitere Faktoren sind die Gasart, der Arbeitspunkt, der Strahlstrom sowie die Geometrie der Extraktionsgitter. Ebenso spielen die inneren Plasmaparameter eine Rolle. Typischerweise liegt die Betriebsfrequenz im hohen kHz- bis einstelligen MHz-Bereich. Der erzeugte Ausgangsstrom hängt von der DC-Versorgungsspannung des RFG ab. Das Hauptziel des RFG ist es, einen maximalen Wirkungsgrad bei der Energieeinkopplung in das Plasma zu erzielen. Um diese Anforderungen zu erfüllen, ist ein hocheffizienter, leistungsstarker RFG entscheidend. Der Aufbau lässt sich in Schaltungstopologien, wie Halb- und Vollbrücke, sowie digitale oder analoge Regelungen klassifizieren. Ein Schwingkreis resultiert aus dem Betrieb des RFG an einer Last, ausgeführt als Serien- oder Parallelschwingkreis [**Jun19**].

Elektromagnetische Verträglichkeit

Elektromagnetische Verträglichkeit ist „die Fähigkeit eines Geräts oder Systems, in seiner elektromagnetischen Umgebung zufriedenstellend zu funktionieren, ohne dabei unzulässige elektromagnetische Störungen zu verursachen“ [**Int18**]. Bei Raumfahrzeugen wird die Situation durch die Anforderungen an ein geringes Gewicht, eine hohe Zuverlässigkeit, Weltraum-umgebung und niedrige Kosten zusätzlich erschwert. Aus diesem Grund sind die üblicherweise verwendeten Ferritabsorber oder eine zusätzliche Abschirmung nicht notwendigerweise zielführend. Daher konzentrieren sich die Entwurfsmethoden, während der Entwicklung, auf das Kabellayout, Gerätedesign und die Anordnung innerhalb der Baugruppe.

Raumfahrzeuge sind typischerweise verschiedenen Umgebungsbedingungen ausgesetzt. Sie interagieren mit ihrer elektromagnetischen Umgebung oder benachbarten Flugkörpern. Beispielsweise sei die Immunität gegenüber elektromagnetischer Strahlung von Radarsystemen und Steuergeräten der Trägerrakete in der Startphase zu nennen. Weiterhin ist die gegenseitige elektromagnetische Beeinflussung von benachbarten Raumfahrzeugen im Orbitalbetrieb zu berücksichtigen [**Zha21**; **Per19**].

Systeme im Inneren von Raumfahrzeugen im Allgemeinen und elektrische Schaltkreise im Besonderen beeinflussen sich gegenseitig. Elektromagnetische Interferenz ist ein wichtiges Thema und wird definiert als eine Beeinträchtigung der Funktionsfähigkeit von Geräten, Übertragungskanälen oder eines Systems aufgrund einer elektromagnetischen Störung. Es gibt mehrere Kopplungspfade zwischen Verursacher- und Opferschaltkreis [**Mon00**]:

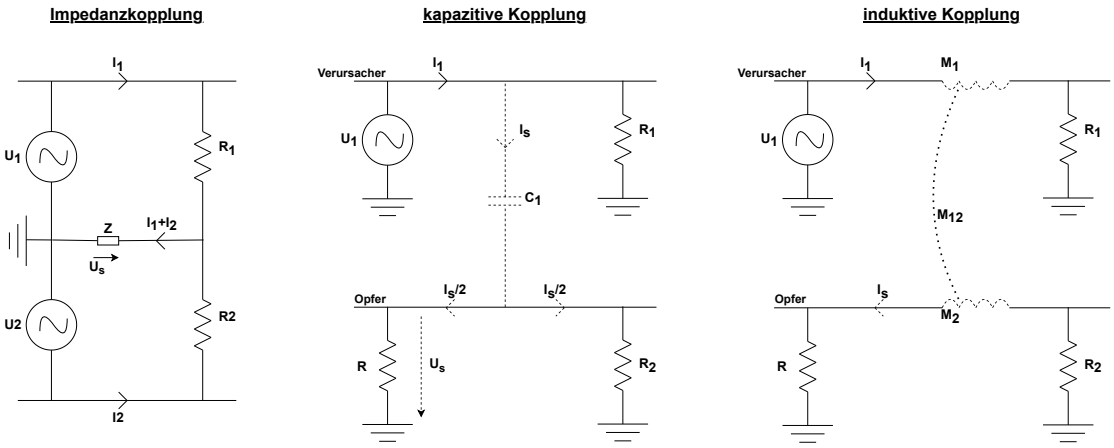

Abbildung 2.1: Leitungs- und feldgebundene (Nahfeld) Kopplungswege der elektromagnetischen Interferenz; I_s bzw. U_s stellen die Störgrößen dar.

- Impedanzkopplung tritt auf, wenn zwei oder mehr Stromkreise eine gemeinsame Impedanz haben, beispielsweise den gleichen Stromrückweg. Die Ströme verursachen an der gemeinsamen Impedanz einen Spannungsabfall, der in den gekoppelten Stromkreisen Störungen verursacht. Dieses Phänomen wird den leitungsgebundenen Emissionen zugerechnet.
- Die kapazitive Kopplung erfolgt durch das elektrische Feld $\vec{E}$. Potentialunterschiede zwischen zwei oder mehreren Stromkreisen bewirken eine Energieübertragung über parasitäre Kapazitäten. Dieses Phänomen wird dem Nahfeld zugeordnet. Die Störgröße ist die sich zeitlich ändernde Spannung $\mathrm{d}u_\mathrm{s}/\mathrm{d}t$.
- Induktive Kopplung entsteht durch das magnetische Feld $\vec{H}$. Zwei oder mehrere benachbarte Stromkreise stören sich gegenseitig durch elektromagnetische Induktion. Die Energieübertragung findet über Koppelinduk-

tivitäten statt. Diese Erscheinung ist ebenfalls dem Nahfeld zuzuordnen. Die Störgröße ist der sich zeitlich ändernde Strom $\mathrm{d}i_s/\mathrm{d}t$.

- Abstrahlung von elektromagnetischen Wellen. Die $\vec{E}$- und $\vec{H}$-Felder sind nicht trennbar, beide Felder sind gekoppelt und bilden elektromagnetische Wellen, welche beispielsweise durch Schwingkreise im Resonanzfall oder durch elektrisch lange Leitungen entstehen. Diese Erscheinung wird dem Fernfeld zugeordnet.

Eine schematische Darstellung der Kopplungspfade findet sich in Abb. 2.1. Befindet sich der Empfänger in der Nähe der Störquelle, werden das elektrische und das magnetische Feld getrennt betrachtet. Dieses Raumgebiet wird als Nahfeld bezeichnet. Wenn der Abstand zwischen Empfänger und Quelle groß ist, liegen Fernfeldbedingungen vor und die elektrischen und magnetischen Felder kombinieren zu elektromagnetischen Wellen [**Ott11**]. Faktoren wie die Quelle selbst, die umgebenden Medien und der Abstand zum Messpunkt prägen das Feld. In geringer Entfernung wird das Feld durch die Quelleneigenschaften charakterisiert. In großer Distanz von der Quelle hängen die Merkmale des Feldes vor allem von dem Medium ab, in dem sich das Feld ausbreitet. Der Raum um die Störquelle lässt sich daher in drei Bereiche unterteilen:

- Das **Nahfeld** befindet sich in der Nähe der Quelle. Der Bereich ist durch Gleichung (2.6) definiert:

$$r \ll \frac{\lambda}{2\,\pi} = \frac{1}{k} \tag{2.6}$$

  Dabei ist

$$\lambda = \frac{c_0}{f}. \tag{2.7}$$

Die Wellenlänge λ und damit die Frequenz f bestimmen den spezifischen Bereich und den maximalen Abstand r zur Störquelle, wobei k die Wellenzahl und c_0 die Lichtgeschwindigkeit ist.

- Der **Übergangsbereich** ist definiert als

$$r \approx \frac{\lambda}{2\pi}. \tag{2.8}$$

- Das **Fernfeld** befindet sich weit entfernt von der Quelle. Die Reichweite wird durch Gleichung (2.9) definiert:

$$r \gg \frac{\lambda}{2\pi} \tag{2.9}$$

Die Literatur definiert den quantitativen Abstand, bei dem das Nahfeld in das Fernfeld übergeht, unterschiedlich. Übliche Werte besagen, dass bis etwa 2λ das Nahfeld und ab etwa 5λ das Fernfeld existiert.

Der Wellenwiderstand, auch Wellenimpedanz genannt, ist das Verhältnis zwischen dem elektrischen und magnetischen Feld. Für das Fernfeld beträgt dieses konstante Verhältnis, das mit Z_0 bezeichnet wird, ungefähr $377\,\Omega$ für Luft und den freien Raum:

$$Z_0 = \frac{E}{H} = \sqrt{\frac{\mu_0}{\epsilon_0}} = 120\,\pi\,\Omega \approx 377\,\Omega \tag{2.10}$$

Dabei ist μ_0 die magnetische Feldkonstante; sie beträgt $4\,\pi \cdot 10^{-7}\,\mathrm{Vs/Am}$. ϵ_0 ist die Dielektrizitätskonstante und nimmt den Wert $8,854 \cdot 10^{-12}\,\mathrm{As/Vm}$ an. Im Nahfeld wird die Wellenimpedanz um weitere Faktoren ergänzt, um auch dort ihre Gültigkeit beizubehalten. Die Parameter hängen von der Quelle selbst und ihrer Entfernung zu dem Bezugspunkt ab. Im Falle eines dominanten elektrischen Feldes (hohe Spannung, geringer Strom) wird die Wellenimpedanz nach Gleichung (2.11) berechnet **[Zha21]**:

$$Z_c = Z_0 \cdot \frac{1}{k \cdot r} = Z_0 \cdot \frac{\lambda}{2 \cdot \pi \cdot r} \tag{2.11}$$

Ist das magnetische Feld dominant (niedrige Spannung, hoher Strom), so ist die Wellenimpedanz durch Gleichung (2.12) gegeben:

$$Z_c = Z_0 \cdot k \cdot r = Z_0 \cdot \frac{2 \cdot \pi \cdot r}{\lambda} \tag{2.12}$$

Elektromagnetische Simulation

Um die Genauigkeit der Vorhersage abgestrahlter Emissionen des Systems bei verschiedenen Betriebspunkten zu erhöhen, wird eine elektromagnetische 3D-Vollwellensimulation (engl. full-wave 3D electromagnetic simulation) durchgeführt. Dadurch lässt sich ein umfassendes Modell einer Baugruppe einschließlich der Peripheriegeräte erzeugen. Die elektromagnetische Vollwellensimulation ermöglicht die Analyse auf Grundlage der Maxwell-Gleichungen ohne Vereinfachungen oder Näherungsformeln. Im Allgemeinen werden zwei Arten innerhalb der Simulationsumgebung unterschieden: Das 3D-Modell, welches

die Geometrie und Materialeigenschaften definiert, und elektrische Schaltungen, welche die Schaltkreise sowie die Funktionsweise von Bauteilen nachstellen. Die Kombination dieser beiden Modelltypen ergibt eine Co-Simulation. Die erzeugten Ergebnisse umfassen diverse Felder und Kopplungsmechanismen. Mit Post-Processing Methoden ist es möglich, weitere Parameter des simulierten Modells zu berechnen.

3 Einordnung der Veröffentlichungen und deren Ergebnisse

Nachfolgend wird der thematische Zusammenhang der Veröffentlichungen aufgezeigt. Eine Einordnung in die Gesamtthematik findet statt. Weiterhin lässt sich der Bezug zum Stand der Wissenschaft herstellen.

3.1 Erste Veröffentlichung

Verification of a radio-frequency generator model in a full-wave 3D EM simulation
Yannik Rover und Chris Volkmar

©2022 IEEE. Reprinted, with permission, from Y. Rover and C. Volkmar, "Verification of a radio-frequency generator model in a full-wave 3D EM simulation", 2022 IEEE Aerospace Conference (AERO), Big Sky, MT, USA, 2022, pp. 1-10, doi: 10.1109/AERO53065.2022.9843355.

Autorenbeiträge

Der korrespondierende Autor Yannik Rover ist für die theoretischen Vorbereitungen sowie die messtechnische Durchführung verantwortlich. Chris Volkmar begleitete das Vorhaben durch Hilfestellungen und Diskussionen. Yannik Rover verfasste den Entwurf des Manuskripts und alle Autoren kommentierten frühere Versionen des Manuskripts. Alle Autoren lasen und genehmigten das endgültige Manuskript. Yannik Rover hielt den zugehörigen Konferenzvortrag.

Einordnung in das Gesamtvorhaben

Ausgehend von dem Stand der Wissenschaft ist ein Simulationsmodell des Radiofrequenz-Generators entstanden. Dieses Modell bildet exakt die mechanische Geometrie samt des Leiterplattenlayouts nach. Kombiniert wird dies mit der Modellierung des Ausgangskreises zur Spulenansteuerung. Die Veröffentlichung beschäftigt sich anschließend mit den Verifikationsmessungen mittels Feldsonden (Nahfeld) und einer GTEM-Zelle (Fernfeld). In einem Frequenzbereich von 100 MHz bis 500 MHz zeigt sich eine gute Übereinstimmung, was die Verwendbarkeit des Simulationsmodells zulässt. In den darüber- und darun-

terliegenden Frequenzbereichen sind die Abweichungen durch die begrenzten Messmethoden zu erklären.

Verification of a radio-frequency generator model in a full-wave 3D EM simulation

Yannik Rover
Center of Competence for Nanotechnology and Photonics (NanoP)
TH Mittelhessen University of Applied Sciences
35390 Gießen, Germany
yannik.rover@ei.thm.de

Chris Volkmar
Center of Competence for Nanotechnology and Photonics (NanoP)
TH Mittelhessen University of Applied Sciences
35390 Gießen, Germany
chris.volkmar@nanop.thm.de

***Abstract*—Ion thrusters, which make an essential part of "NewSpace" missions, play a major role in spacecraft systems for propulsion and maneuvering. Therefore, the thrusters and their peripherals must be safe and reliable. Furthermore, the mutual interference of active high-frequency components – such as the radio-frequency generator (RFG) typically used with RF ion thrusters – and satellite components regarding immunity and emissions must be considered. The RFG provides the energy for the thruster coil and thus controls the operating point of the thruster – which makes it a very crucial part of a radio-frequency ion thruster (RIT) assembly. Here, we propose procedures to obtain the radiated emissions of the RFG in the near and far field, respectively. For this purpose, partial procedures are adapted from a standard. A comparison of the two measurement environments - near and far field - is sought via calculations of the radiated power. The paper also examines discrepancies between the curves as well as the unexpected results and provides explanations. An outlook is given on how the acquired measurement data will help in the verification of a previously created full-wave 3D EM simulation model of the RFG.**

TABLE OF CONTENTS

1. INTRODUCTION

Nowadays, electric thrusters are important propulsion systems in space. Increasing commercialization has a major impact on space flight and especially on electric propulsion (EP). Strong reasons for emerging space travel are scientific, political, military and economic objectives. The still existing challenges are leading to extensive research in energy efficiency, electromagnetic compatibility (EMC), alternative propellants, and scalability, to name a few [1].

Additional information on EP and for further work is given in section 2. Section 3 describes the fundamentals of electrical quantities and physical effects used for measurement and calculation in section 5. The measurement setup is shown in section 4. The results of the measurements performed are presented and discussed in section 6. Finally, a conclusion summarizing the work is given in section 7.

2. MOTIVATION AND BACKGROUND

Ion thrusters, which make an essential part of "NewSpace" missions, play a major role in spacecraft systems for propulsion and maneuvering. Therefore, the thrusters and their peripherals must be safe and reliable. In addition to functionality, electromagnetic compatibility requirements must also be met to always ensure stable operation under all operating conditions. Furthermore, the mutual interference of active high-frequency components – such as the radio-frequency generator typically used with RF ion thrusters – and satellite components regarding immunity and emissions must be considered. In fact, the electronics (including the RFG) constitute about 60 % of the total thruster assembly, which shows the importance of examinations of those "peripheral" components and their interaction with the thruster itself and other satellite components.

Radio-frequency Ion Thruster

Radio-frequency ion thrusters are part of the electric thruster family. Each thruster in space is based on the recoil principle. There are different ways to generate thrust, in case of electric thrusters there are three physical principles [1]:

- **Electrothermal** thrusters heat the gas electrically. Thrust is generated by thermodynamical expansion of the gas.
- **Electrostatic** thrusters ionize the propellant with a high-frequency rf-energy coupling. The charged ions are accelerated by an electrostatic field. A RIT is a representative of this group of thrusters.
- **Electromagnetic** thrusters use a static magnetic field via permanent magnets to ionize and accelerate the gas. These two processes cannot be controlled separately.

The radio-frequency ion thruster and all electric thrusters in general use electrical energy for their operation. In contrast,

978-1-6654-3760-8/22/$31.00 ©2022 IEEE

2022 IEEE Aerospace Conference (AERO) | 978-1-6654-3760-8/22/$31.00 ©2022 IEEE | DOI: 10.1109/AERO53065.2022.9843355

chemical thrusters use the chemical binding energy of the propellant. Electrical energy is available through the solar panels, but is limited for technological reasons such as energy storage or power electronics efficiency. The ejection velocity of the ions is limited for the same reasons. Currently, the ejected ions reach a speed of 30 to 50 kilometers per second. This is about ten times higher than the ejection velocity of chemical thrusters. Therefore, electric thrusters have a higher mass efficiency - a better ratio of thrust per unit mass of propellant [1].

These positive characteristics are accompanied by two disadvantages: First, ion thrusters operate only in high vacuum and not under atmospheric pressure, so it is not possible to launch from a planet. Second, the thrust is very low; in the range of micronewtons to about half a newton. This is due to the limitation of electrical power. Therefore, the ion thrusters demonstrate their benefits in space at low gravity.

Radio-frequency generator

The radio-frequency generator is the focus of current research. It provides energy for the thruster coil and thus controls the operating point of the thruster – making it a very crucial part of a RIT assembly. The RFG output provides a high frequency sinusoidal current for inductive coupling of electrical energy into the plasma. The frequency range depends on the geometry of the ionization vessel and coil. In addition, inner plasma parameters and peripheral component losses play a role. Typically, the operating frequency is in the high kHz to single-digit MHz range. The associated output current depends on the set input voltage.

The main goal of the RFG is to achieve maximum efficiency in energy conversion. To fulfill these requirements, a highly efficient, high performance RFG is crucial. The RFG consists of a digital controller, implemented as a field-programmable gate array (FPGA), ensuring precise timing and fast tracking of the optimal resonant frequency. Furthermore, a half- or full-bridge design allows for control of the varying output load [2].

Simulation model

In order to increase predictability of the radiated emissions of the system and during different operating points, a full-wave 3D electromagnetic simulation is created to obtain a comprehensive model of a RIT assembly including RFG. The simulation model of the RIT thruster already exists. In the case of the peripherals, the RFG is now being replicated. The 3D model of the RFG comprises housing, connections to the outside and PCB layouts. The internal electronic devices are represented by schematics and Spice models. The combination of these two types of models results in a co-simulation. The outputs generated include the magnetic and electric fields as well as the farfield radiation. With post-processing, it is possible to calculate even more parameters of the simulated model. The radiated power is an example of this and a factor for later verification of the model. In figure 1 the 3D model is shown. The modeling and simulation are done with the SIMULIA CST STUDIO SUITE software.

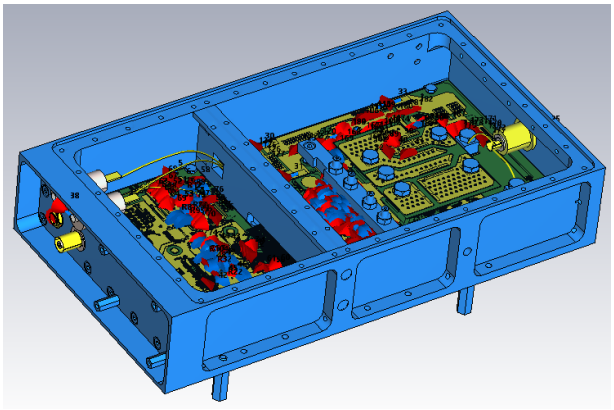

Figure 1. Simulation model of the current RFG development.

3. THEORY

Electromagnetic compatibility is ”the ability of an equipment or system to function satisfactorily in its electromagnetic environment without introducing intolerable electromagnetic disturbances to anything in that environment.”[3] EMC technology for spacecraft is based on traditional theory. For spacecraft, the situation is further complicated by requirements on weight, reliability, space environment, and cost. For this reasons, the commonly used ferrite absorbers or an additional shielding may not be the first choice. Therefore, design methods should focus on bonding, grounding, routing and cable layout. Since spacecraft are typically subject to various operating conditions, e.g., integration testing, launch, and on-orbit operation, special attention should be paid to the effects of these conditions on the electromagnetic environment (EME). Hence, the EMC characteristics of the spacecraft are associated to its EME [4].

Inner spacecraft systems, in general, and electrical circuits, in particular, affect each other adversely. Electromagnetic interference (EMI) is an important issue and is defined as a degradation in the performance of equipment, transmission channels, or a system due to an electromagnetic disturbance. There are several coupling paths between the culprit and victim circuit [5]:

- **Capacitive** coupling occurs due to the electric field $\vec{E}$. Differences in potential between the culprit and victim circuits cause energy transfer. This phenomenon is assigned to the near field.
- **Inductive** coupling occurs due to the magnetic field $\vec{H}$. Two or more adjacent circuits interfere with each other due to electromagnetic induction. This phenomenon is assigned to the near field.
- **Impedance** coupling occurs if two or more circuits have a common impedance, such as the same return path. The currents cause a voltage drop that can interfere with the other circuit. This phenomenon is assigned to the conducted emissions.
- **Radiation** of electromagnetic waves. The E- and H-fields cannot be separated, both fields are coupled to form electromagnetic waves. This phenomenon is assigned to the far field.

The poynting-vector $\vec{S}$ is defined as the density and direction of energy transport of an electromagnetic field. It is perpendicular to the electric and magnetic field as shown in equation 1 [6].

$$\vec{S} = \vec{E} \times \vec{H} \tag{1}$$

The handling of the electric and magnetic field depends on various conditions. If the receiver is located close to the source of the noise, the electric and magnetic fields are considered separately. This is called the near field. If the distance between the receiver and the source is large, the far field is reached and the electric and magnetic fields combine to form electromagnetic waves [7].

Factors such as the source, the surrounding media and the distance to the point of interest characterize the field. At a small distance from the source, the field is characterized by the properties of the source. At a great distance from the source, the qualities of the field depend primarily on the medium in which the field propagates. The space around the noise source can therefore be divided into three areas:

- The **near field** is located near the source. Its range is defined by equation 2. The wavelength λ and thus the frequency f determine the specific range and the maximum distance r to the source of noise.

$$r \ll \frac{\lambda}{2\,\pi} = \frac{1}{k} \tag{2}$$

with

$$\lambda = \frac{c_0}{f} \tag{3}$$

where k is the wave number and c_0 is the speed of light.
- The **transition region** is in the range where the wavelength divided by 2π is approximately equal to the distance to the noise source.
- The **far field** is located far away from the source. Its range, which is inverse to the near field, is defined by equation 4.

$$r \gg \frac{\lambda}{2\,\pi} = \frac{1}{k} \tag{4}$$

The wave impedance is the ratio of the electric field to the magnetic field. For the far field, this ratio, called characteristic impedance Z_0, is approximately $377\,\Omega$ for air and free space:

$$Z_0 = \frac{E}{H} = \sqrt{\frac{\mu_0}{\epsilon_0}} = 120\,\pi\,\Omega \approx 377\,\Omega \tag{5}$$

where μ_0 is the magnetic permeability and is given as $4\pi \cdot 10^{-7}$ Vs/Am. ϵ_0 is the permittivity (dielectric constant) and is given as $8.854 \cdot 10^{-12}$ As/Vm. In the nearfield, this ratio is not constant, but depends on the source and the distance between the source and the point of interest. In case of a dominant electric field (high voltage, low current) the wave impedance is calculated using equation 6. If the magnetic field is dominant (low voltage, high current), the wave impedance is given by equation 7 [7].

$$Z_\mathrm{c} = Z_0 \cdot \frac{1}{k \cdot r} = Z_0 \cdot \frac{\lambda}{2 \cdot \pi \cdot r} \tag{6}$$

$$Z_\mathrm{c} = Z_0 \cdot k \cdot r = Z_0 \cdot \frac{2 \cdot \pi \cdot r}{\lambda} \tag{7}$$

4. Methodology and Measurement Setup

Two power supplies and an output load are required for RFG operation. In addition, current and field probes are necessary to determine the operating point and for field detection, respectively. Figures 2 and 3 show the arrangement of the equipment for the measurement in the near and far field, respectively.

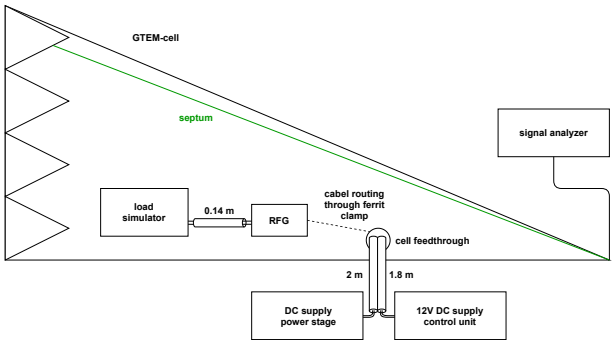

Figure 2. Arrangement of the equipment for far field measurements.

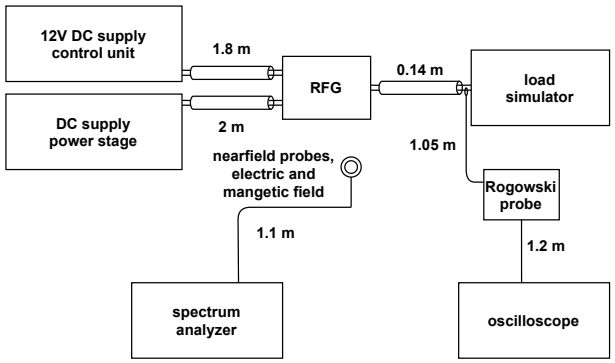

Figure 3. Arrangement of the equipment for near field measurements.

The RFG is an in-house development from prior research work [8]. The half-bridge design is used for the measurements. The power supply for the control board of the RFG is a standardized supply with an output voltage of 12 V DC. The supply for the intermediate circuit is a dc voltage source from ET System with the model designation LAB/SMP 2150. The output range is 0 V to 150 V DC, 0 A to 16 A, and the maximum power is 2400 W. The load simulator is an in-house development and replicates the thruster coil by adjustable inductance and resistance. The inductance and resistance range is 3 µH to 6 µH and 0 Ω to 6 Ω, respectively. The wiring between the devices is done with triaxial cables.

The further equipment is used for measurements and has the following properties: The spectrum analyzer is a Rohde&Schwarz FPC 1500 with a frequency range of 3 GHz, used for near field measurements. In combination with the GTEM cell a signal analyzer Agilent Technologies N9000A with a frequency range from 9 kHz to 7.5 GHz is used. The oscilloscope is a Tektronix MDO3104 with a frequency range of 1 GHz and a sampling rate of 5 GS/s. A rogowski sensor from PEM with the model designation CWTUM/03/B is used for current measurement, the peak current is 60 A. The field probes for magnetic and electric field sensing are probes from

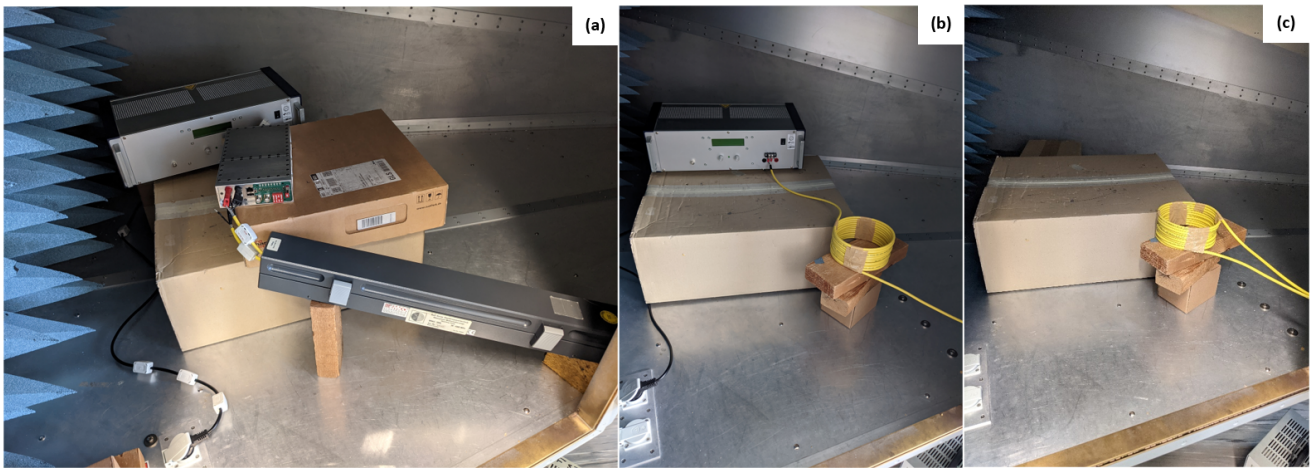

Figure 4. GTEM cell configurations: (a) load simulator and RFG inside, (b) load simulator and cable inside, (c) cable inside

EMCO with model number 7405-902 (3 cm loop probe for magnetic field, 1 MHz to 500 MHz) and number 7405-904 (ball probe for electric field, 100 kHz to 500 MHz).

A Gigahertz Transverse Electromagnetic (GTEM) cell is required for far field measurements. This is a shielded enclosure with the ability to test radiated emission (RE) and radiated susceptibility (RS). From an electrical standpoint, the GTEM cell is an extended 50 Ω transmission line. The mechanical geometry of the housing is in the shape of a pyramid and represents the outer conductor. The septum is the inner conductor in which the radiated fields of the equipment under test (EUT) generate a measureable voltage. Reflections and resonance phenomena are eliminated by RF absorbers and a 50 Ω termination between the housing and the septum [6].

5. Measurement and Calculation

After completion of modeling and simulation, the main objective is to verify the simulation results. For verification, it is mandatory to perform experiments on the real RFG. This is done either with a GTEM cell in which the RFG and the associated components are inserted, or with near field probes. The various operating points are as follows: The inductance is constant at 3 µH, the resistance varies between 0.5 Ω and 1.4 Ω. The output current is given to 2 A, 3 A and 6 A, respectively.

Far field (GTEM cell)

Figure 4 shows the three measurements in the GTEM cell for far field radiation. First, the RFG in combination with the load simulator is inside the cell and both contribute to the measured emissions. In another setup, the RFG powers the load simulator from outside the cell. Thus, only the load simulator and the connected cable are inside the cell. The last setup consists of only the cable, RFG and load simulator are outside the cell. This is done to obtain the influence of the cable to calculate the emissions of the load simulator. The cable is wound to a coil, because of the necessity to have always the same arrangement in the cell to get a good comparison between the setup cable and load simulator (b) and only cable (c). In case of the load simulator, the wiring comes from the cell feedthrough and goes to the load simulator with about 11 windings. When the load simulator is outside the cell, the cable comes from the feedthrough and goes back to the load simulator with 10.5 turns. Except for the half winding, the cable setup is similar to the previous measurement and can be compared and calculated accordingly.

The emissions from the devices under test (DUT) cause a voltage on the septum which is measured with a signal analyzer. The internal interference sources can be simplified as Hertzian dipoles, so it is necessary to align the DUT in three different orientations. All dipole structures are taken into account and can be combined into one voltage using equation 8:

$$V = \sqrt{V_{\mathrm{p1}}^2 + V_{\mathrm{p2}}^2 + V_{\mathrm{p3}}^2} \tag{8}$$

where V is the total voltage composed of the voltages of the individual dipol orientations U_{px}. A correlation algorithm establishes the relationship between the voltage on the septum and the electric field in the far field. The final equation for determining the electric field is shown in appendix A and depends on the maximum E-field in vertical and horizontal polarization. The complete correlation algorithm is also included in this appendix. For this calculation, the field factor of the cell, the polarization factors and the dimensions of the cell are required. The result is a frequency-dependent electric far field that can be compared to limits in a standard or even to check simulation models. This process is implemented in software and directly connected to the signal analyzer of the GTEM cell and its measured data. Another important indication is the radiated power of the DUT. This can be calculated with the voltage on the septum and another correlation (Eq. 9):

$$P = \frac{Z_0}{3\pi} \cdot \frac{k^2}{e_{0\mathrm{y}}^2} \cdot Z_{\mathrm{c}} \cdot V^2 \tag{9}$$

where P is the radiated power and e_{0y} is the TEM field factor of the GTEM cell. Now there are already two data sets that can be used for simulation verification. With the results of the three setups (a), (b) and (c), it is possible to obtain only the radiation of the RFG. This eliminates the unwanted radiation

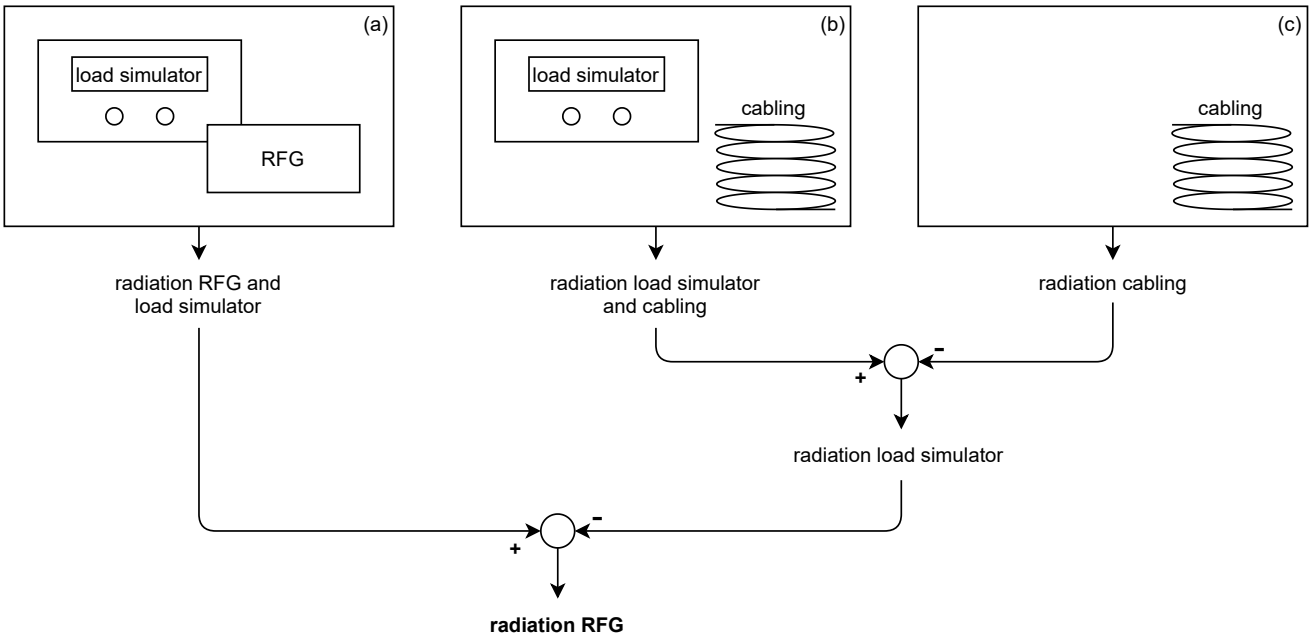

Figure 5. **Calculation procedure for obtaining the radiation of the RFG.**

contributions from the cabling and the load simulator. Figure 5 shows the process for determining the RFG radiation.

Near field (field probes)

The near field measurements are performed with the same operating points as the far field measurements. The electric and magnetic fields are obtained by field probes. These probes are moved above the RFG and as close as possible above the cover. The reason is the comparison with the far field measurements, where the radiated power of the RFG is calculated. The radiated power calculated from the near field should thus also be in close proximity to the RFG. The measured voltage is combined with the antenna factor of the probe used and the magnetic or electric field is obtained. Eqs. 10 and 11 show the resulting field strength as a function of the antenna factor of the probes. The antenna factor diagram of the respective probe used can be found in appendix B.

$$H_{\mathrm{dB\mu A/m}} = V_{\mathrm{dB\mu V}} + AF_{\mathrm{dB}} \tag{10}$$

$$E_{\mathrm{dB\mu V/m}} = V_{\mathrm{dB\mu V}} + AF_{\mathrm{dB}} \tag{11}$$

The radiated power in the near field is calculated to:

$$\begin{aligned} P &= H \cdot E \cdot A_{\mathrm{RFG}} \cdot \frac{A_{\mathrm{RFG}}}{A_{\mathrm{measured}}} \\ &= H \cdot E \cdot A_{\mathrm{RFG}} \cdot f \end{aligned} \tag{12}$$

where A_{RFG} is the total area of the RFG housing. f is a factor that indicates the ratio between the total area of the RFG housing and the area on which the measurement points are obtained. The assumption that the radiation is isotropic leads to measurements on a certain area and the extrapolation in the calculation. Due to the lack of spatial orientations, it is permissible to use only the magnitudes of the fields and neglect their spatial dependence. On the one hand, the near field results can be used for simulation verification in the form of comparisons. On the other hand, mutual verification is achieved with the calculated radiated powers of the near and far field.

6. Results and Discussion

The generated data have to be defined and incorporated into the investigations. The operating points with $6\ \mathrm{A_{RMS}}$ output current are neglected in this discussion, because of the necessary high input power of the RFG. In combination with the coil-shaped cabling, the power stage of the RFG cannot be operated in safe state. Furthermore the RFG indicates that it cannot find the resonant frequency properly.

Far field

First, the GTEM cell is not a perfect conductor and has tiny slots into which the electromagnetic waves from the environment couple. The ambient radiation consists, for example, of FM radio ($100\,\mathrm{MHz}$) or the mobile phone network ($800\,\mathrm{MHz}$). Due to the measurement setup, the background noise is additionally increased by power supplies and measurement components, called peripheral noise. The both radiations are also indicated in the plots and are subtracted from the actual radiation for the later evaluations. The first measurements correspond to an operating point with a load of 3 µH and $0.5\,\Omega$ and an output current of $3\ \mathrm{A_{RMS}}$. Figure 6 shows the emissions of the three configurations (a), (b) and (c). These measurements show the electric field strength data in the far field.

With the generated data, the emissions of the RFG can be calculated. This is done using the procedure shown in figure 5. The resulting emissions can be seen in figure 7. There are some missing data points in the curve. This can be explained

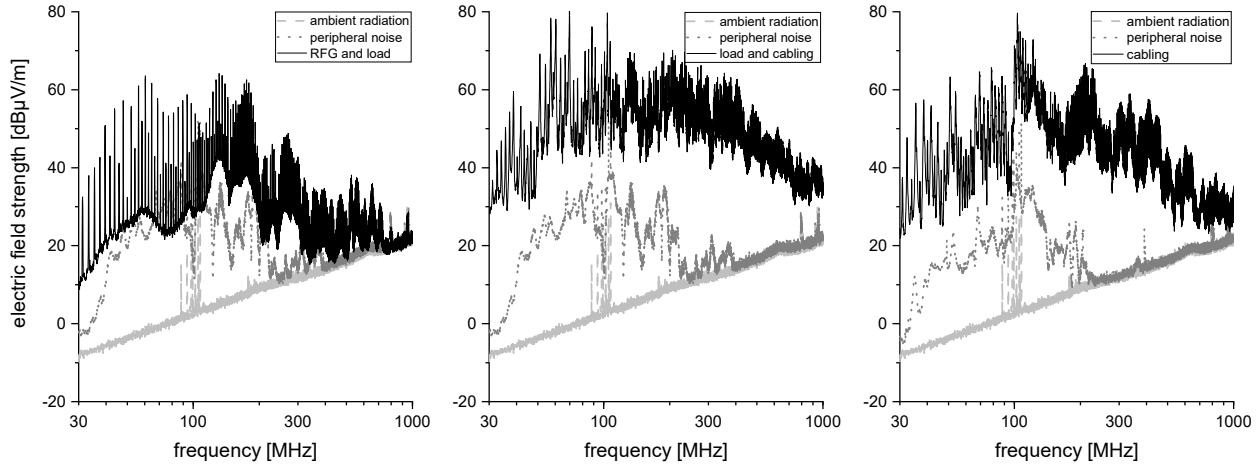

Figure 6. Measurements of the three configurations in the GTEM cell. The output current is 3 A_{RMS} with a load of 3 µH and 0.5 Ω.

as follows: The ambient radiation can change during the measurement period, depending on the ambient noise level at this moment. Also, the load simulator has a tolerance of about 30 % and its behaviour depends on the current load as well as the temperature. Therefore, the calculated negative field strenghts are set to NaN in the linear range. There is no possibility to represent a negative value in the logarithmic scale. In addition to that, the RFG has a display which signals the desired resonant operation. If this matching indicator does not light up, more radiation can occur because there is no defined operating point for the RFG.

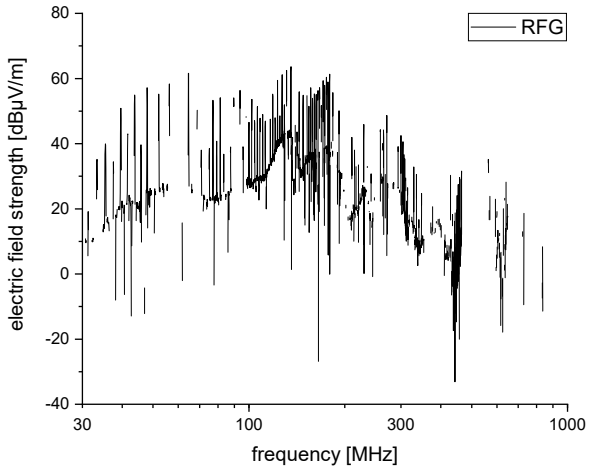

Figure 7. Calculation of the electric field strength emitted by the RFG. The output current is 3 A_{RMS} with a load of 3 µH and 0.5 Ω.

From the electric field strength of the RFG follows directly the radiated power. It is shown in figure 8. The radiated power is also missing some data points, since the electric field strength of the RFG forms the basic data. For a better comparison with the near field measurements, the curve is smoothed with the Savitzky-Golay method.

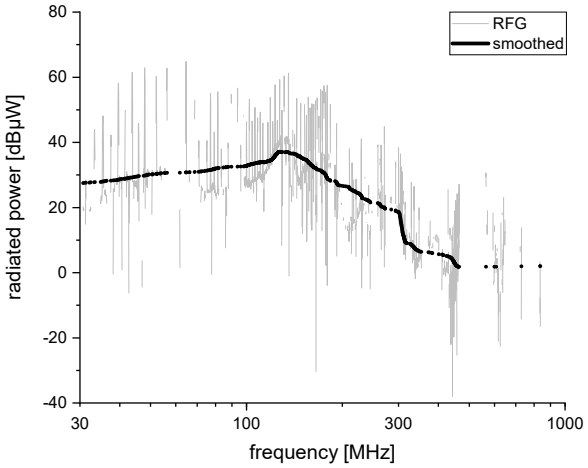

Figure 8. Calculation of the radiated power of the RFG. The output current is 3 A_{RMS} with a load of 3 µH and 0.5 Ω.

Near field

In the near field, the measurements are done with the magnetic and electric field probes. In figure 9 the electric and magnetic field strengths are shown. The radiated power is shown as well and calculated with the field strengths. It should be considered that the near field measurements were not performed in a shielded room. All the near field plots show a peak at about 1.84 MHz. It is the resonant frequency of the output circuit and the switching frequency of the power stage.

Near and far field comparison

The radiated power is used to compare the near and far field measurements. These curves are shown in figure 10. In general the curves follow the same directions with an offset in the far field radiated power.

For more measurement data, appendix C includes the comparison with a load of 3 µH and 1.4 Ω. This load is supplied with an output current of 2 A_{RMS} and 3 A_{RMS}, respectively.

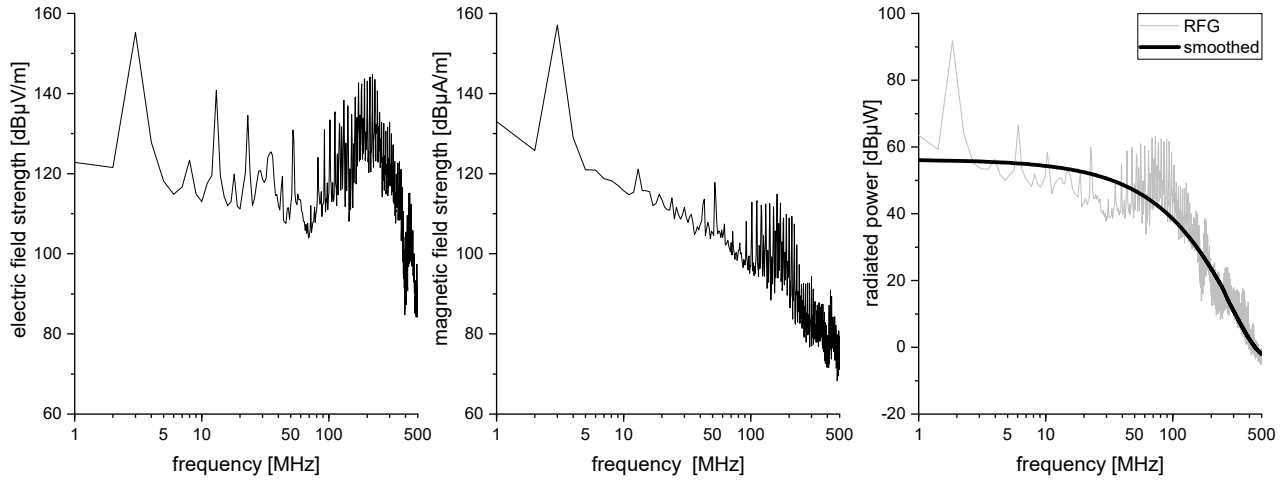

Figure 9. **Near field measurements of the electric and magnetic field of the RFG as well as the calculation results of the radiated power. The output current is 3 A_{RMS} with a load of 3 µH and 0.5 Ω.**

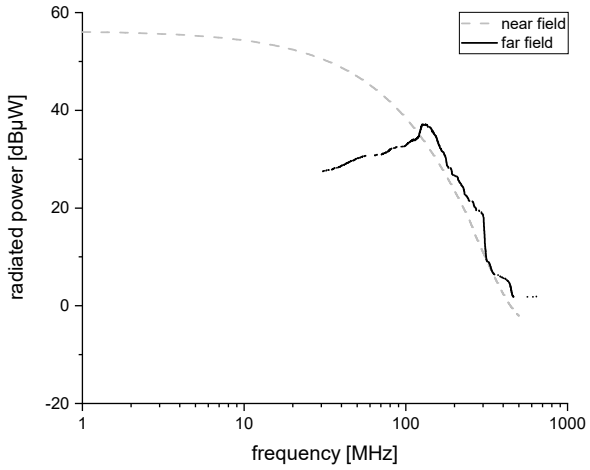

Figure 10. **Calculated radiated power from the near and far field measurements. The output current is 3 A_{RMS} with a load of 3 µH and 0.5 Ω.**

Both electric far fields as well as the comparison of the radiated power at 2 A_{RMS} are shown. At this operating point, both radiated powers show no good agreement. The level of agreement depends on the operating point.

The deviations can be explained as follows:

- **Ambient radiation:** As explained earlier, the ambient radiation changes over time as random frequency applications occur outside. The GTEM cell is not completely sealed, EM waves enter through tiny slots. The near field measurements are not performed in a shielded room. The ambient radiation and also the interference with other peripherals distort the measurements.
- **Antenna factor:** The characteristic curve of the antenna factor is not available in tabular form. Therefore, reading deviations occur in the lower single-digit dB range.
- **Cabling and loops:** In GTEM cell configuration (a), the RFG supply cables are still in the GTEM cell. There is no way to eliminate them. The emissions from the cabling are reduced by a ferrite clamp. Furthermore, the wiring in configurations (b) and (c) is not exactly the same, in one setup there is half a winding less and the cabling is arranged slightly differently.
- **Isotropic radiation:** The calculations assume that the radiation is isotropic and that all sides of the RFG have the same emissions. Furthermore, only the top side is measured with the field probes. The total radiated power is extrapolated in the algorithm.
- **Load simulator tolerance:** The load simulator consists of switching relays to adapt the desired impedance. It has a tolerance of about 30 % and its behaviour depends on the current load as well as the temperature.
- **Matching frequency:** The RFG strives for the resonant frequency and this point indicates its optimal working range. If the resonant frequency is not reached, the RFG operates in a state where it tries to find the resonant frequency with various adjustments of the output stage. As a result, it cannot be assumed that the radiated power increases with the output power of the RFG. Even lower output currents at the same load can lead to a comparatively higher radiated power. Observations have shown that the resonant frequency was sometimes matched and sometimes not, regardless of a particular operating point or an repeatable procedure.
- **Radiation directions:** The emissions of the RFG that exit from the bottom of the RFG are reflected by the ground in the GTEM cell and contribute to the voltage at the septum. In the near field, these emissions do not contribute to the measured voltage and are only included in the calculation when the RFG surface is used ($\rightarrow$ Isotropic radiation).

Nevertheless it is a good first approach to combine near and far field measurements and thus verify simulation results. In the frequency range between 100 MHz and 500 MHz, the curves show good agreement. Therefore, it can be assumed that the near and far field measurements used to verify the simulation are valid over the total frequency range. It can be seen that above 500 MHz, both curves increase. In the frequency range below 100 MHz, the curves diverge drastically and exhibit inverted characteristics. This is due to the complex near field characteristics, where the field strengths are not proportional to the measured distance r, but depend quadratically or even cubically.

7. CONCLUSION AND OUTLOOK

In this paper, a method was presented that compares near and far field emissions of an RFG. By applying and advancing the procedure in the standards, good agreement is achieved at certain operating points and frequency ranges. The establishment of different configurations in the GTEM cell led to the possibility of calculating only the far field emissions of the RFG. Extending the Poynting vector with a suitable radiating surface led to a comparable radiated power in the near field. All in all, the results show usable and comparable data. In case of deviations and unexpected curves, the assumptions and reasons were described. Further investigation of deviations below $100\,\mathrm{MHz}$ will be conducted.

The next steps are to verify the simulation model with the generated data of the measurements. The simulation model calculates electromagnetic quantities such as the electric and magnetic field strengths in the near field, the radiated power as well as the far field emissions. All quantities are already measured, calculated and verified. If suitable matches are found, the RFG simulation model can also be unified with the existing RIT model. In this way, cable arrangements and interference effects can be investigated.

APPENDICES

A. CORRELATION ALGORITHM FOR FAR FIELD CALCULATIONS

The correlation algorithm follows the standard "DIN EN 61000-4-20 (VDE 0847-4-20): 2011-07".

Algorithm equations

The radiated power of the DUT is given to:

$$P_0 = \frac{Z_0}{3\pi} \cdot \frac{k^2}{e_{0y}^2 \cdot Z_c} \cdot V^2 \tag{13}$$

The combined voltage of the septum, calculated with the dipole orientations, is:

$$V = \sqrt{V_{p1}^2 + V_{p2}^2 + V_{p3}^2} \tag{14}$$

The determination of the TEM field factor is done either with a measurement for a known device, equation 15, or with the geometrical dimensions of the cell in equation 16:

$$e_{0y} = \frac{E_y(x,y)}{\sqrt{P_i}} \tag{15}$$

$$e_{0y} = \frac{4}{a} \cdot \sqrt{Z_c} \cdot sum \tag{16}$$

with

$$sum = \sum_{m=1,3,5,\ldots}^{\infty} \left[\frac{\cosh(My)}{\sinh(Mh)} \cdot \cos(Mx) \cdot \sin(M\frac{a}{2}) \cdot \mathrm{J}_0(Mg) \right] \tag{17}$$

and

$$M = m\frac{\pi}{a} \tag{18}$$

The geometrical factor to obtain the horizontal and vertical electric field is as follows:

$$\begin{aligned} g_{\text{max,hor}} &= \left| \frac{e^{-jk_0 r_1}}{r_1} - \frac{e^{-jk_0 r_2}}{r_2} \right|_{\max} \\ &= \left| \frac{1}{r_1 r_2} \left[r_2^2 + r_1^2 - 2r_1 r_2 cos(k_0(r_2 - r_1)) \right]^{1/2} \right|_{\max} \end{aligned} \tag{19}$$

$$\begin{aligned} g_{\text{max,ver}} &= \left| \frac{s^2}{r_1^2} \frac{e^{-jk_0 r_1}}{r_1} + \frac{s^2}{r_2^2} \frac{e^{-jk_0 r_2}}{r_2} \right|_{\max} \\ &= \left| \frac{s^2}{r_1^3 r_2^3} \left[r_2^6 + r_1^6 - 2r_1^3 r_2^3 cos(k_0(r_2 - r_1)) \right]^{1/2} \right|_{\max} \end{aligned} \tag{20}$$

with

$$r_1 = \sqrt{s^2 + (R_H - h_g)^2} \tag{21}$$

$$r_2 = \sqrt{s^2 + (R_H + h_g)^2} \tag{22}$$

The maximum electric field depending on the distance s is calculated to:

$$\begin{aligned} E_{\max} &= g_{\max} \cdot \sqrt{\frac{3Z_0}{4\pi} P_0} \\ &= g_{\max} \cdot \frac{Z_0 \cdot k_0}{2\pi \cdot e_{0y}} \cdot \frac{V}{\sqrt{Z_c}} \end{aligned} \tag{23}$$

Nomenclature and dimensions

Symbol	Identifier	Dimension
a	cell width	m
e_{0y}	TEM field factor	$\sqrt{\Omega}/m$
E_{max}	electric field	V/m
E_y	electric field	V/m
g	gap septum and cell wall	m
g_{max}	horizontal and vertical polarisation	m
h	septum height	m
h_g	DUT height groundplane	m
J_0	0^{th} order Bessel function	
k_0	wave number	$1/m$
M		$1/m$
P_0	radiated power DUT	W
P_i	input power DUT	W
r_1	distance DUT receiving antenna	m
r_2	distance virtual DUT receiving antenna	m
R_H	receiving antenna height groundplane	m
s	distance receiving antenna	m
V	combined septum voltage	V
V_{px}	septum voltage (dipole x=1,2,3)	V
x,y,z	DUT position	m
Z_0	characteristic (wave) impedance	Ω
Z_c	wave impedance	Ω

B. ANTENNA FACTOR

EMCO 7405-902

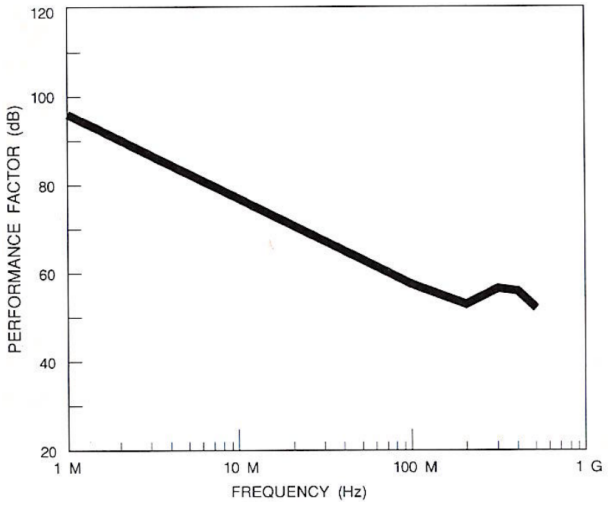

EMCO 7405-904

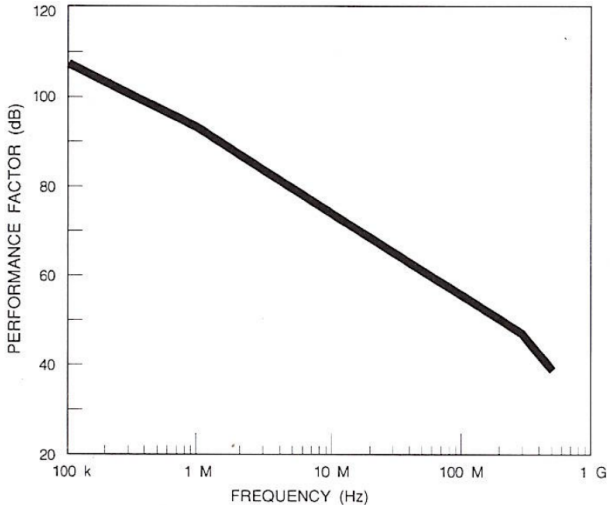

C. Additional measurement data

Electric field strenghts of the RFG with an output load of $3\,\mu H$ and $1.4\,\Omega$:

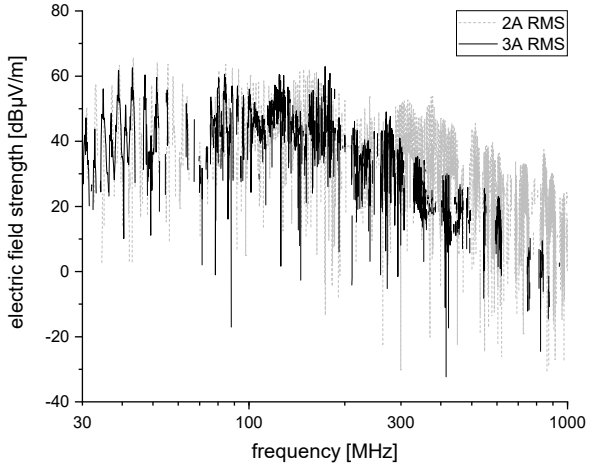

Radiated power of the RFG with an output load of $3\,\mu H$ and $1.4\,\Omega$ at $2\ A_{RMS}$:

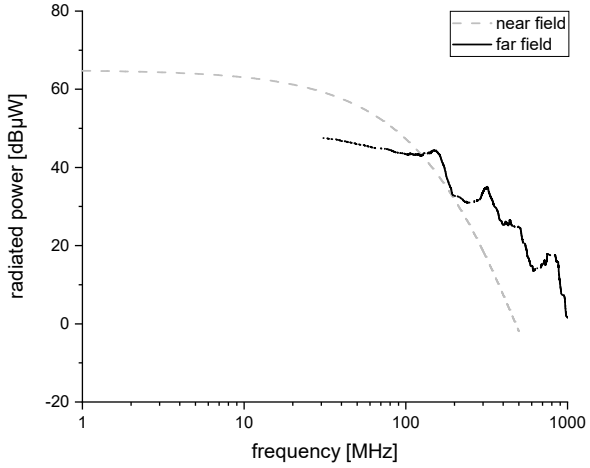

References

[1] Holste, K., et al., "Ion thrusters for electric propulsion: Scientific issues developing a niche technology into a game changer", Rev. Sci. Instrum. 91, 061101 (2020), https://doi.org/10.1063/5.0010134

[2] Junker, J. E., Probst, U., Klar, P. J., "Development of a full bridge series resonant radio-frequency generator for optimized RIT operation", IEPC-2019-474 (2019), University of Vienna, Austria

[3] International Electrotechnical Commission, "IEC standard 60050-161-01-07: International Electrotechnical Vocabulary: Electromagnetic compatibility: Basic concepts", 2018

[4] Zhang, H., et al., "Spacecraft Electromagnetic Compatibilities Technologies", Springer (2021), ISBN 978-981-15-4781-2, https://doi.org/10.1007/978-981-15-4782-9

[5] Montrose, M. I., "Printed Circuit Board Design Techniques for EMC Compliance: A Handbook for Designers", Wiley (2000), ISBN 0-7803-5376-5

[6] Perez, R. J., "Handbook of Aerospace Electromagnetic Compatibility", Wiley (2019), ISBN 978-111-89-1051-1

[7] Ott, H. W., "Electromagnetic Compatibility Engineering", Wiley (2011), ISBN 978-0470189306

[8] Simon, J., Probst, U., Klar, P. J., "Development of a Radio-Frequency Generator for RF Ion Thrusters", IEPC-2015-289 (2015), Hyogo-Kobe, Japan

Biography

Yannik Rover *received his B.Eng. and M.Sc. degrees in Electrical Engineering from TH Mittelhessen University of Applied Sciences and Hochschule Darmstadt University of Applied Sciences, respectively. He is currently working as Ph.D. student at the University of Gießen in cooperation with TH Mittelhessen University of Applied Sciences. His interests include electromagnetic compatibility in the field of electric propulsion.*

Chris Volkmar *received his B.Eng. and M.Sc. degrees in Electrical Engineering from TH Mittelhessen University of Applied Sciences and his Ph.D. in Physics from the University of Gießen in 2015. He led the metrology group for electric propulsion at the German Aerospace Center. As professor for EP and EMC he is the co-head of the Space Electronics work group at TH Mittelhessen University of Applied Sciences.*

3.2 Zweite Veröffentlichung

Modeling the influence of an electric thruster's ion beam on its global EMC
Yannik Rover, Rainer Thüringer, Uwe Probst und Chris Volkmar

©2023. Reprinted, with permission, from Y. Rover, R. Thüringer, U. Probst and C. Volkmar, "Modeling the influence of an electric thruster's ion beam on its global EMC", Front. Space Technol. 4:1287474 (2023), https://doi.org/10.3389/frspt.2023.1287474; Creative Commons Attribution 4.0 International License: https://creativecommons.org/licenses/by/4.0/, no changes made.

Autorenbeiträge

Der korrespondierende Autor Yannik Rover ist für die Forschung verantwortlich. Er erstellte die Simulation, führte die Ionenstrahlmodellierung durch und untersuchte die Ergebnisse. Chris Volkmar leistete wichtige Unterstützung bei der Modellierung und Auswertung der Verifikation. Rainer Thüringer, Uwe Probst und Chris Volkmar unterstützten diese Arbeit durch Diskussionen und Vorschläge für neue Ansätze. Yannik Rover verfasste den Entwurf des Manuskripts und alle Autoren kommentierten frühere Versionen des Manuskripts. Alle Autoren lasen und genehmigten das endgültige Manuskript.

Einordnung in das Gesamtvorhaben

Um die Simulationsmodelle des RFG und des RIT-4 weiter zu vervollständigen, ist der Ionenstrahl in nachfolgender Veröffentlichung simuliert worden. Die Ergebnisse zeigen die Auswirkungen verschiedener Konfigurationen und Arbeitspunkte, wie bespielsweise Divergenzwinkel, Gitterspannung oder Ansteuerungssignale der Spule. Der Neutralisator, der eine wesentliche Funktion für den Betrieb eines Ionentriebwerks einnimmt, wurde bei dieser Arbeit vernachlässigt. Vorerst soll der Einfluss des Ionenstrahls an sich beleuchtet werden,

außerdem ist die entstehende Elektronenwolke des Neutralisators diffus und daher durch ein einfaches Modell erster Ordnung nicht konkret darstellbar. Eine Möglichkeit der Einbeziehung der Elektronen in den Ionenstrahl besteht in der Nutzung eines Drude-Modells, die Homogenität der Elektronen wird dabei angenommen. Das Resultat spiegelt den Ionenstrahl und dessen effektive Leitfähigkeit wieder.

In einer nachfolgenden Forschungsarbeit lässt sich der Neutralisator und die damit verbundene Elektronenextraktion, zur Neutralisierung des Ionenstrahls, untersuchen. Dazu sind folgende Arbeitsschritte möglich: Die Elektronenentladung wird durch die Bildung einer Plasmabrücke mit dem Ionenstrahl des Triebwerks gekoppelt. Die aus dem Neutralisator extrahierten Elektronen fließen über diese Plasmabrücke und neutralisieren so den Ionenstrahl [**Hol20**]. Dabei muss die Gesamtladung der Elektronen ungefähr der Summe der Ionenladungen entsprechen, um die Neutralität zu gewährleisten.

Lan und Kaganovich [**Lan20**] zeigen die Entwicklung der Teilchendichte während der Neutralisierung des Ionenstrahls. Zunächst dehnt sich der Ionenstrahl aus und schrumpft im Zuge der Neutralisierung wieder, siehe dafür Abb. 2 in [**Lan20**]. Aufgrund der Potentialverteilung befinden sich die Elektronen zunächst in der Mitte des Ionenstrahls. Der Neutralisierungsvorgang füllt den gesamten Ionenstrahl anschließend zunehmend mit Elektronen. Da dieser transiente Vorgang lediglich einige Mikrosekunden andauert, ist es legitim, direkt die Modellierung des Endstadiums durchzuführen. Weiterhin wird in den Ergebnissen deutlich, dass die transversale Position des Neutralisators einen erheblichen Einfluss auf die Neutralisierung des Ionenstrahls hat.

Usui, Hashimoto und Miyake [**Usu13**] führen eine Particle-In-Cell Simulation durch und zeigen ebenfalls die Ionen- und Elektronenverteilung im zeitlichen und örtlichen Verlauf. Durch Verluste und Interaktionsmechanismen zwischen Ionenstrahl und Elektronenentladung wird der Ionenstrahl nicht vollständig neutralisiert.

Einen weiteren Anhaltspunkt liefern die Messungen an der halb-reflexionsfreien Anlage mit einem RIT-4. Die elektromagnetische Vermessung diverser Arbeitspunkte dokumentiert die im Rahmen eines studentischen Projektes durchgeführten Arbeiten. Das RIT-4 ist in der Kammer aufgebaut und angeschlossen, der RFG versorgt die Spule des Triebwerks über eine vier Meter lange Triaxialleitung von außen. Die Versorgung des Gittersystems ist ebenfalls von außen über ein Leitungssystem sichergestellt. Zum Vergleich zwischen Messung und Simulation wird folgender Arbeitspunkt gewählt:

- RIT-4 mit einem Massenfluss von $0,3\,\mathrm{sccm}$ Xe. Der Gitterstrom beträgt $7\,\mathrm{mA}$ bei einer Gitterspannung von $U_{\mathrm{PHV}} = 900\,\mathrm{V}$ sowie $U_{\mathrm{NHV}} = 0\,\mathrm{V}$.
- RFG mit einer Eingangsspannung von $18,55\,\mathrm{V}$ für den Leistungskreis, ausgeführt als Vollbrücke, und einer Betriebsfrequenz von $1,8\,\mathrm{MHz}$.

Die Parametrisierung des Simulationsmodells erfolgt mit den Werten des Arbeitspunkts. Der Vergleich bildet einen Frequenzbereich von $65\,\mathrm{MHz}$ bis $1\,\mathrm{GHz}$ ab. Die Ergebnisse in Abb. 3.1 zeigen, dass die gemessenen Emissionen (2) im oben genannten Arbeitspunkt geringer sind als die in der Simulation (4). Die Differenz liegt je nach Frequenzpunkt im unteren zweistelligen Dezibel-Bereich.

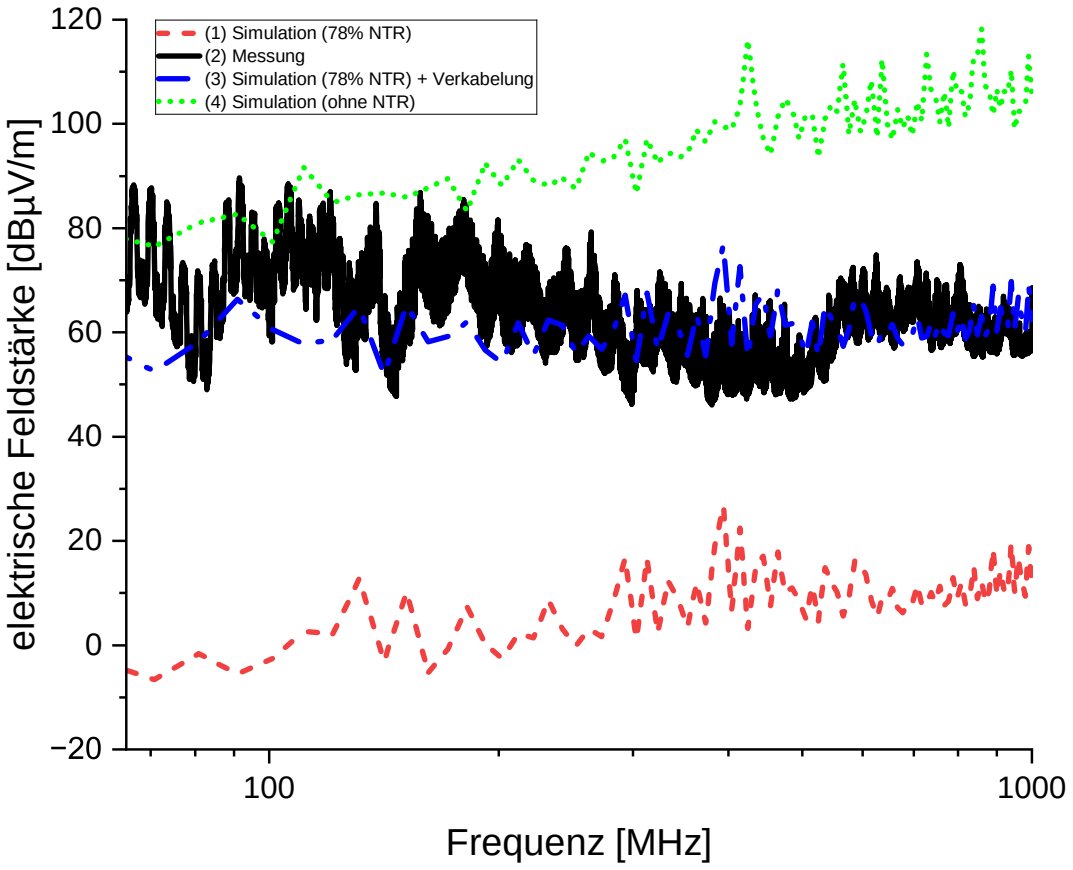

Abbildung 3.1: Vergleich der Emissionen im Fernfeld zwischen Messung und Simulation im Arbeitspunkt mit einem Massenfluss von 0,3 sccm Xe und einem Gitterstrom von 7 mA. Die Gitterspannungen liegen bei 900 V (PHV) und 0 V (NHV). Der RFG Leistungskreis wird mit 18,55 V bei einer Frequenz von 1,8 MHz betrieben. Die Messentfernung beträgt 2 m. Die schwarze Kennlinie zeigt die Emissionen der Messung innerhalb der SAC. Weiterhin wird das Ergebnis der Simulation (78 % Neutralisierungsgrad) in rot wiedergegeben. Der blaue Verlauf zeigt die Simulationswerte in Kombination mit realitätsnahen Leitungsemissionen (60 $\mathrm{dB}_{\mu\mathrm{V/m}}$). Die Ergebnisse der Simulation ohne Neutralisierung des Ionenstrahls spiegeln sich in der grünen Kurve wider.

Eine Erklärung liefert die bei normalem Triebwerksbetrieb in der Absorberkammer vorhandene Neutralisation des Ionenstrahls. Wird die Neutralisation in der Simulation berücksichtigt (78 % Neutralisierungsgrad), verringern sich die simulierten Emissionen ebenfalls deutlich. Die nun resultierende Differenz zwischen (1) und (2) in Abb. 3.1 wiederum lässt sich auf Störemissionen der Verkabelung zurückführen. Bei vergleichbarem Betrieb werden Werte von bis zu $80\,\mathrm{dB}_{\mu\mathrm{V/m}}$ erreicht [**Rov22**]. Wird der Einfluss der Versorgungsleitungen mit in die Simulationsergebnisse einbezogen (siehe (3) in Abb. 3.1), entsteht eine gute Übereinstimmung zwischen Simulation und Messung. Die Frequenzverläufe stimmen überein. Die quantitativen Abweichungen werden durch Messunsicherheiten sowie Rauschen erklärt. Eine Unsicherheit stellen die Emissionen der Verkabelung dar, die hier lediglich basierend auf vorherigen Forschungsarbeiten angenommen, aber nicht gemessen wurden. Weiterhin lässt der Divergenzwinkel des Ionenstrahls Unsicherheiten zu. Dieser wurde bei den Messungen nicht bestimmt, ist jedoch innerhalb der Simulation ein entscheidender Faktor [**Rov23**].

frontiers | Frontiers in Space Technologies

TYPE Methods
PUBLISHED 27 November 2023
DOI 10.3389/frspt.2023.1287474

Check for updates

OPEN ACCESS

EDITED BY
Jochen Schein,
Bundeswehr University Munich, Germany

REVIEWED BY
Maximilian Maigler,
Munich University of the Federal Armed Forces, Germany
Daisuke Kuwahara,
Chubu University, Japan

*CORRESPONDENCE
Yannik Rover,
yannik.rover@nanop.thm.de

RECEIVED 01 September 2023
ACCEPTED 25 October 2023
PUBLISHED 27 November 2023

CITATION
Rover Y, Thueringer R, Probst U and Volkmar C (2023), Modeling the influence of an electric thruster's ion beam on its global EMC.
Front. Space Technol. 4:1287474.
doi: 10.3389/frspt.2023.1287474

COPYRIGHT
© 2023 Rover, Thueringer, Probst and Volkmar. This is an open-access article distributed under the terms of the Creative Commons Attribution License (CC BY). The use, distribution or reproduction in other forums is permitted, provided the original author(s) and the copyright owner(s) are credited and that the original publication in this journal is cited, in accordance with accepted academic practice. No use, distribution or reproduction is permitted which does not comply with these terms.

Modeling the influence of an electric thruster's ion beam on its global EMC

Yannik Rover*, Rainer Thueringer, Uwe Probst and Chris Volkmar

Center of Competence for Nanotechnology and Photonics (NanoP), TH Mittelhessen University of Applied Sciences, Giessen, Hesse, Germany

This research deals with electromagnetic compatibility (EMC) in the field of electric propulsion (EP). To complete previous investigations, the emissions of a fully operating radio-frequency thruster (RIT)—including its extracted ion beam—were numerically analyzed. The ion beam was simulated and investigated with various characteristics. The simulations were performed by means of transient co-simulation. It is clear that the ion beam had a significant impact on the thruster emissions. Properties such as divergence angle and the conductivity of the beam, which can be directly attributed to the operating point of the plasma discharge inside the thruster, play a major role. The next steps will be to bring together all the knowledge gained about the emissions of the individual thruster components as well as the peripheral electronics.

KEYWORDS

electric propulsion, electromagnetic compatibility, simulation, far field, ion beam, radiofrequency ion thruster

1 Introduction

Traditionally, electric thrusters have been primarily used for station-keeping and orbit attitude control missions. Nowadays, electric thrusters are also used as propulsion systems for orbit raising and space travel. Increasing commercialization has a great impact on space flight—especially on electric propulsion systems. Scientific, political, military, and economic goals present strong reasons for the emerging demand for space flight. The challenges that still exist are leading to extensive research in areas such as energy efficiency, electromagnetic compatibility, alternative propellants, and scalability (Holste et al., 2020).

Electromagnetic compatibility (EMC) is "the ability of an equipment or system to function satisfactorily in its electromagnetic environment without introducing intolerable electromagnetic disturbances to anything in that environment" (International Electrotechnical Commission, 2018). Spacecraft EMC technology is based on traditional theory but is further complicated by weight, reliability, the space environment, and cost requirements. Since spacecraft are typically subject to various operating conditions, such as integration testing, launch, and on-orbit operation, special attention should be paid to the impact of these conditions on the electromagnetic environment (EME). Therefore, the EMC characteristics of the spacecraft are related to its EME (Zhang et al., 2021). To meet these requirements, a holistic understanding of the EMC of a thruster assembly is required. Some parts of the thruster assembly have been analyzed separately. In past studies, for example, a radio-frequency generator was investigated for its EMC by simulation and measurement (Rover and Volkmar, 2022). It became clear that the supply lines and cabling to the thruster are the decisive influencing factors from an EMC point of view. Furthermore, a semi-anechoic vacuum chamber was designed and set up at our department and is described in a

previous publication (Rover et al., 2023). There seem to be no recent studies or substantial research results related to the electromagnetic interference (EMI) of an ion beam.

The device tested was a radio-frequency ion thruster, where the designation RIT-4 indicates the 4-cm diameter of the grid extraction system. We have analyzed and reported here the influence and EMI characteristics of the thruster, including its extracted ion beam, in order to complete the investigation of individual thruster areas. We also validated the general use of the simulation environment.

The motivation of this research is presented in Section 2. Section 3 describes the environment of the simulation where the thruster and the ion beam were examined. Additional features and model characteristics are introduced in Section 4. Section 5 shows the validity of the simulation environment, and thus the accuracy of the results, using physical principles and mathematical analyses. Results and comparisons of different operating points are presented in Section 6, including best practice. Finally, Section 7 summarizes the work and its outputs and provides an outlook.

2 Motivation

Ion thrusters, which are an essential part of "NewSpace" missions, play an important role in spacecraft propulsion and maneuvering systems. These thrusters and their peripherals must therefore be safe and reliable. In addition to functionality, electromagnetic compatibility requirements must be met to ensure stable operation under all operating conditions. Furthermore, the mutual interference of active high-frequency components—such as the radio-frequency generator typically used in RF ion thrusters—and satellite components must be taken into account in terms of immunity and emissions. Electronics comprise about 60% of the total thruster assembly, which indicates the importance of studying these supposedly "peripheral" components and their interaction with the thruster and other satellite components.

3 Simulation approach

The simulation consisted of a 3D model and an electrical circuit, called *schematic* in the simulation process. The 3D model represented the physical conditions of the object under investigation. The schematic generated and fed the supply signals as well as further electrical elements.

The simulation was performed with *SIMULIA CST Studio Suite* software version *2023 SP5* from *Dassault Syste mes*. A full-wave 3D electromagnetic simulation was performed in order to increase the predictability of the radiated emissions of the system during different operating conditions. In this type of simulation, all Maxwell equations are solved without any simplifying assumptions. The 3D model consisted of mechanical components such as the thruster itself as well as models of the discharge plasma and extracted ion beam. The neutralizer was an important part of the thruster and its operation. In this research, it was disregarded because the resulting electron cloud is diffuse, and, therefore, a simple first-order model is not sufficiently concrete. Accordingly, only the ion beam was first characterized, providing sufficient accuracy for the model. During the ground tests in our laboratories, the setup was also often operated without a neutralizer; we thus had a first comparable indicator with the model. However, any realistic space scenario would dictate the use of a neutralizer. Therefore, this research should be understood as a first step toward a holistic EMC simulation approach.

The electronic components and control signals are defined in the schematic tab. The combination of these two types of modeling produces a transient co-simulation—an alternative to the standard simulation. The standard process uses S-parameters to describe the 3D model for any combination of port excitations. Their calculation requires either a frequency sweep (frequency-solver) or a simulation per port (time-solver). In transient co-simulation, on the other hand, only one simulation of the coupled circuit is performed, where the excitation is defined in the schematic tab. Fortunately, the 3D model and the schematic were solved simultaneously, so interactions and mutual influences between the 3D model and the schematic were taken into account. In the standard simulation, however, S-parameters are first derived from the 3D model and are then linked to the schematic part. Accordingly, the transient co-simulation was used.

In conducted disturbances, the near and far field are important quantities within EMC. These areas can be addressed with the model shown. Here, the individual case of the far field and the interaction and effect of the thruster and extraction beam were explored to complete the previous research. To obtain the simulated far-field electrical characteristics, it was necessary to place field monitors and field probes at the desired distance from the model (source). Their position depended on the desired frequency range as well as the desired accuracies. In this project, a frequency range of 0–1 GHz was considered. Above 30 MHz, the radiated disturbances usually dominate the conducted disturbances (European cooperation for space standardization, 2012), so we focused on the radiation's impact on the results. As field probes monitored the radiated powers, post-processing allowed calculation of the electrical field strengths of the far field. Transient signals defined in the schematic excited the 3D model, and signal type, amplitude, and frequency could be set.

Post-processing calculations as well as the defining shape and spatially resolved conductivity of the ion beam were performed using *MATLAB* software version *R2022a* from *The MathWorks, Inc*. The basis of the beam conductivity calculation is the distribution function of the ions; their relevant descriptive parameters depend on assumptions of grid and plasma properties. According to Figure 1, the ion beam consisted of volume elements that model the beam shape and allow spatially resolved individual conductivity settings. If the parameters changed, the ion beam was recalculated.

The model permitted us to test various operating points of the thruster and obtain the radiation characteristics of the thruster with an active ion beam. This enabled preliminary checks to be made on the EMC behavior of a fully operating thruster at specific operating points.

4 Modeling

4.1 3D model

The 3D model included the RIT-4, the plasma, and also the ion beam (Figure 1). The RIT-4 model and the plasma modeling had been set up in a previous work (Baruth, 2017); the dimensions and

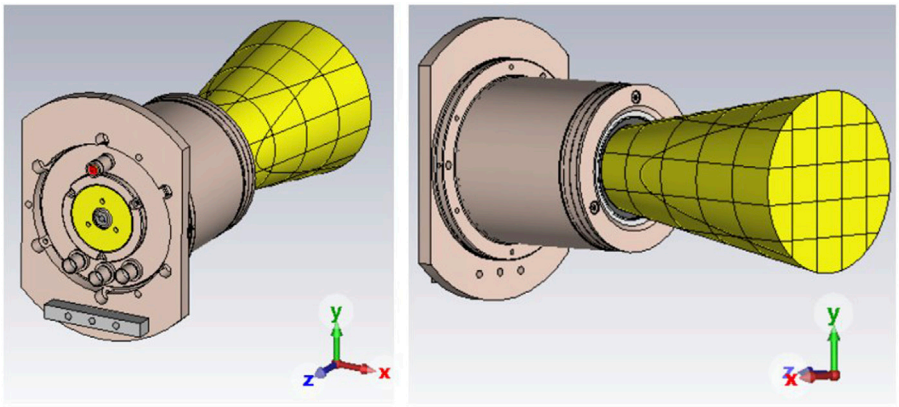

FIGURE 1
Modeling of RIT-4 and ion beam.

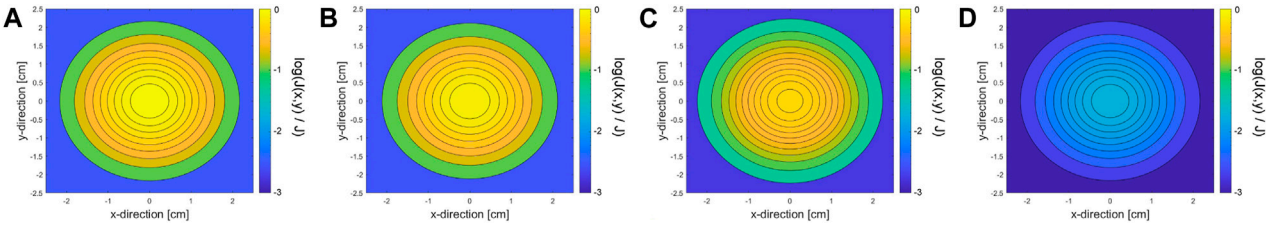

FIGURE 2
Normalized ion density distribution in the x–y plane at varying axial distance downstream from the thruster grid: **(A)** at the extraction grid, **(B)** at 1/3 length of the ion beam, **(C)** at 2/3 length of the ion beam, **(D)** at the end of the simulated ion beam.

materials were defined and assigned to its components. In order to consider the plasma from an electrotechnical point of view, its dielectric properties were determined. For this purpose, a Drude plasma was used (Chabert and Braithwaite, 2011). In the simulation model, a material with the appropriate dielectric properties could be created and placed in the interior of the ionization vessel to mimic the behavior of a real plasma to a certain extent— sufficiently accurate for EMC analyses. The plasma conductivity mainly depended on these parameters:

- electron plasma frequency ω_{pe} (with electron density n_e),
- effective impact frequency $\nu_{m,eff}$,
- excitation frequency ω.

These parameters can be determined by simulation or experiment. However, this requires self-consistent models that are specifically tailored to low-temperature plasmas. The determination was carried out in Baruth (2017).

4.2 Ion beam

The ion beam was also represented by materials of different conductivities. First, the density was calculated based on the spatial distribution of the ions inside the beam. As can be seen in Figure 2, the density number decreases along the ion beam with the square distance to the extraction grid, as in Eq. 1:

$$\rho \propto \frac{1}{z^2}. \tag{1}$$

The location-dependent densities $J(x, y)$ and $J(z)$ are related to total density J on the grid. From the center of the beam, the density decreases outward according to a Gaussian profile. The application of the Gaussian profile is also subject to boundary conditions: the far-field condition approximates the representation of the current density by a plane wave. The standard deviation in the far field of the ion distribution is determined by Eq. 2:

$$\sigma = \frac{z}{2.4477} \cdot \tan\alpha. \tag{2}$$

Here, σ is the standard deviation, z the ion beam length, and α the divergence angle. A value of 2.4477 follows from the calculation of the chi-square distribution of second degree (Reynolds, 1971). Another condition is keeping a certain ratio of the beam length to the radius R_0 of the extraction grid to ensure far-field beam conditions, as in Eq. 3:

$$\frac{z}{R_0} = 6 \ldots 8. \tag{3}$$

Eqs 4, 5 were used to calculate the current density J and conductivity κ:

$$J = \frac{I}{A} = q \cdot n \cdot v, \tag{4}$$

$$\kappa = \frac{J \cdot z}{V}. \tag{5}$$

Here, J is the current density, I the ion beam current, A the grid area, κ the conductivity, and V the high voltage at the extraction grids. The current density was calculated for the grid area. Due to the ion distributions in the z-direction and in the x–y plane (Figure 2), the current density was adjusted by the distribution functions at the further positions in the ion beam.

When determining the current, the charge of a single ionized xenon particle is $q = 1e = 1.602 \cdot 10^{-19}$ As and its mass is $m = 131.293$ u with mass unit $u = 1.66054 \cdot 10^{-27}$ kg. It is assumed to be constant, as well as the velocity v, which depends on the grid voltage V according to Eq. 6:

$$v \approx \sqrt{\frac{2 \cdot q \cdot V}{m}}. \tag{6}$$

With $V = 1$ kV, the velocity is $v \approx 38.335$ km/s.

There are a number of state-of-the-art modeling approaches with corresponding tools for simulating ion optics. The limitation of computing power led to the electrons being calculated with the Boltzmann relation (fluid) and not as particles (PIC approach), and only one beamlet was simulated (Becker and Herrmannsfeldt, 1992; Kalvas et al., 2010; Reeh et al., 2017). There are approaches to simulating the entire extraction system including the beam; very large computational requirements (computational clusters) are necessary because there is insufficient information about the actual beam. The current beam profile depends on the curvature of the grids and also on the plasma density distribution in the ionization vessel (Dobkevicius and Feili, 2016; Reeh et al., 2019). The model is based on empirical values. We thus used a first-order model that can also commonly be found in the literature (Goebel and Katz, 2008) and that could be validated in empirical experiments (Scholze et al., 2019).

First, cubes of equal size were generated, each assigned to a material with individual calculated conductivity. Then, a cone shape was formed using the divergence angle. The ion beam was created when the cone shape and cubes overlapped. The better the discretization, the more accurate the replication. For reasons of low calculation time and project size, a discretization of five steps per axis was used. Accordingly, there were up to 125 cubes to model the ion beam (Figure 1). Using an application programming interface (API), the ion beam was created directly with *MATLAB* commands in the *CST* environment. The API (Symeonidis, 2018) used was extended with modified methods and new functionalities, such as setting project properties, creating shapes, and combining materials and shapes.

4.3 Electronics and control

The schematic tab represents the electrical components and control system (Figure 3). The RFG drive signal was a square wave with a given frequency and maximum value. A capacitance was connected, which completed the actual resonant circuit. The value of 2.27 nF was chosen because of a known and used RFG; a realistic value for a coil inductance of the RIT-4 is 1.2 µH. Using Eq. 7, the optimum excitation frequency is calculated:

$$f = \frac{1}{2 \cdot \pi \cdot \sqrt{L \cdot C}}. \tag{7}$$

A cable simulation was also included. The cable was located between the output circuit of the control and the coil port of the RIT-4 model. The cable simulation included geometric data of the triaxial cable used. The length was set to 0.65 m. All other data such as the material of the conductor or insulation are given according to the data sheet of the cable type *Belden* 9,222 *Triax*.

5 Verification

The goal of verification is to check the simulation results using analytical equations. To ensure the validity of the simulation, a known and computable antenna structure is modeled: the Hertzian dipole. It is used to calculate the electric far field at a given distance r by applying an analytical equation. First, this equation was derived. Second, the simulation software *CST* was used to simulate the dipole structure. Its results were compared with the analytical solution.

The Hertzian dipole is a fictional construct intended to simulate two oscillating point charges; the theoretical equations for electric fields are derived from it. Accordingly, this construct can represent any electrical far-field situation. From an electromagnetic point of view, every structure acts like three orthogonal dipoles (Figure 4). The design, size, and excitation of each dipole depend on the situation describing the emissions; they are independent of each other. The ideal Hertzian dipole is an infinitesimal short current element, which generates the same radiation as an electrically long wire, such as with $l = \lambda/2$. At integer multiples of $\lambda/2$, the radiation is maximal (Kark, 2016). Thus, it is a theoretical construct that enables validation of the solver and the simulation; a possible replica is shown in Figure 5. For structures of length dl, traversed by alternating current i and frequency f, the electric field strength is calculated according to Eq. 8, depending on the distance r to the dipole (in main radiation direction) (Gustrau, 2015):

$$\mathrm{d}E_{\max} \approx \mathrm{d}E_{\theta} = Z_0 \cdot \frac{i \cdot \mathrm{d}l \cdot f}{2 \cdot c_0 \cdot r}. \tag{8}$$

Here, $Z_0 = 120\pi\,\Omega$ is the characteristic impedance in the far field, and $c_0 \approx 300 \cdot 10^6$ m/s is the speed of light in vacuum. The composition of the fields will be discussed in order to understand this relationship. In the near field, field strengths exist depending on the angle θ and ϕ, as well as the radial component r (spherical coordinates). In the far field, the radial component is neglected because there is nearly a plane wave, and therefore, the electric field depends on θ. This becomes clear in Figure 6. The shape is created as the field lines exit at one end of the dipole and enter at the other.

The approximation in Eq. 8 assumes the most ideal boundary conditions, which can only be produced to a limited extent in *CST*. It is valid just in the far-field range and for short antenna structures (Gustrau, 2015), as in Eq. 9:

$$l \ll \frac{\lambda}{10} = \frac{c_0}{10 \cdot f}. \tag{9}$$

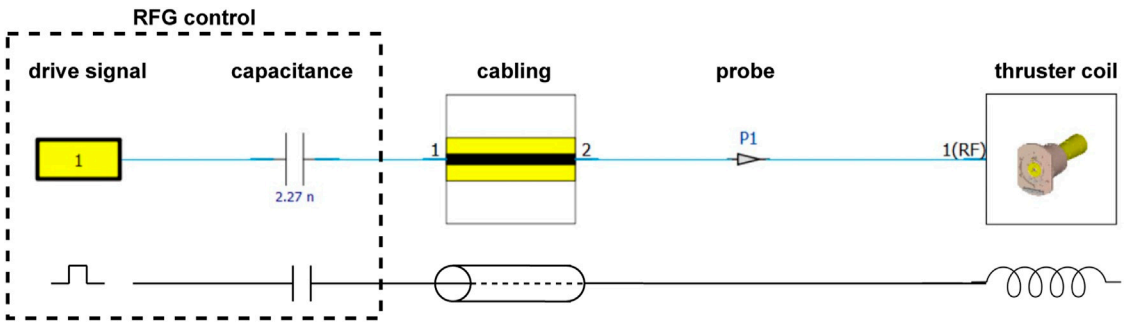

FIGURE 3
Schematic tab of the simulation with illustrative symbols.

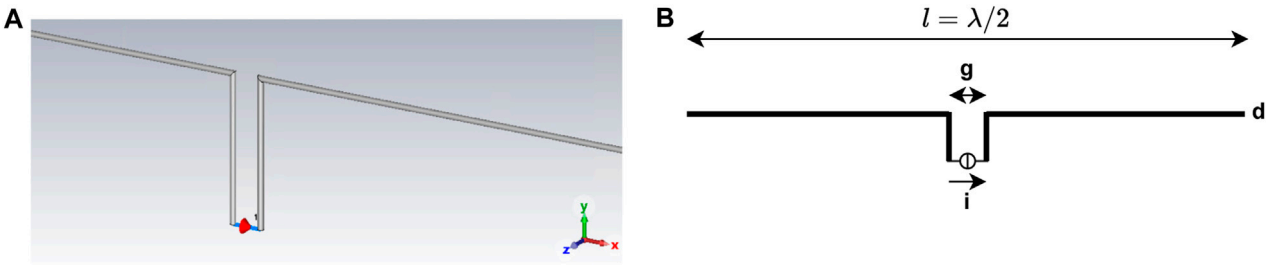

FIGURE 4
Electric dipole: **(A)** CST verification model, **(B)** schematic view of the ideal dipole.

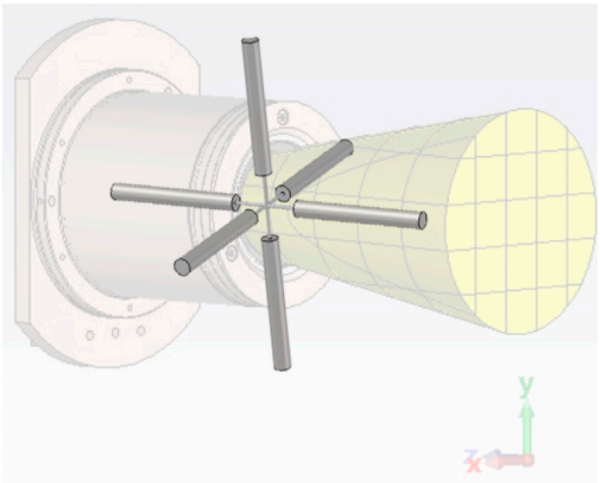

FIGURE 5
Use of a Hertzian dipole structure for electromagnetic representation of the thruster model's emission (schematic view).

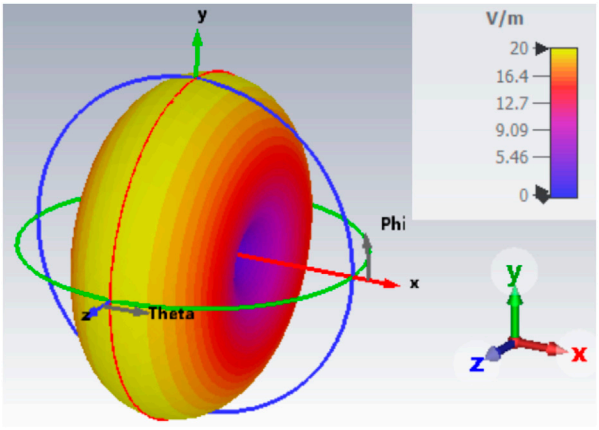

FIGURE 6
3D electric far-field emissions of a Hertzian dipole in r =3 m distance and $l = \lambda/2$ (resonance). Dipole orientation in the x-direction.

Here, λ is the wavelength. The verification environment, including all settings, is the same as that of the thruster model. The dipole's assigned material is a perfect electric conductor, since Eq. 8 also assumes an optimal structure. The excitation is a current source with 1 A. The ideal Hertzian dipole structure has a total length of $l = \lambda/2$ in order to reach maximum radiation. This length is possible despite the condition from Eq. 9 because a real dipole can be concatenated from several ideal Hertzian dipoles. To validate the verification model, a comparison of the thus far ideal (theoretical) and a replicated dipole is necessary. To do this, the mechanical length of the replicated dipole must be adjusted because of the finite

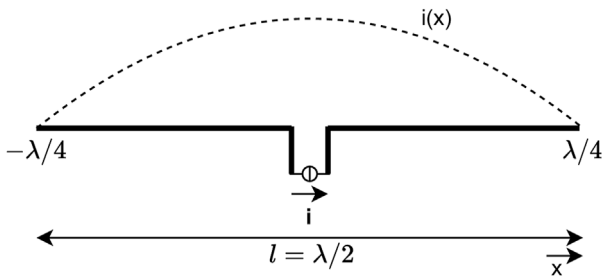

FIGURE 7
Current coverage of a Hertzian dipole at resonance. Dipole orientation in the *x*-direction.

thickness d of the wire as well as the spatial environment. This correction is achieved with the multiplication factor A, which depends on the ratio of the wavelength to the cable diameter d respective to gap g of the dipole (Figure 5). The ratio of wavelength to diameter in the verification is $\lambda/d = 1{,}000$, while for the gap applies a ratio of $g = \lambda/200 = 0.05 \cdot \lambda$. This results in a multiplication factor of $A \approx 0.95$ according to Fig. 11.18 in Kark (2016). The mechanical length of the dipole as the verification model is calculated according to Eq. 10:

$$l_m = A \cdot l = A \cdot \frac{\lambda}{2}. \tag{10}$$

The distance of the far-field measurements is $r = 3$ m. The consideration happens at $l \ll r$ since the far-field conditions are fulfilled here. Furthermore, the observation takes place in the resonance case, where the maximum phase position is analyzed. To use Eq. 8 for this verification case, a derivation is necessary: in the resonance case, the current coverage on the ideal dipole is exactly one sine half-wave (Jackson, 1998) (Figure 7). Thus, the current on the dipole depends on the ongoing position according to Eq. 11:

$$i(x) = \hat{i} \cdot \cos(k \cdot x), \tag{11}$$

where k is the wave number and can be calculated via $\frac{2\pi}{\lambda}$. This current behavior inserted at Eq. 8 results in Eq. 12:

$$E_{max}(r) \approx \frac{Z_0}{2 \cdot \lambda \cdot r} \cdot \int i(x)\,dx = \frac{Z_0 \cdot \hat{i}}{\lambda \cdot r} \cdot \int_0^{\lambda/4} \cos(k \cdot x)\,dx. \tag{12}$$

The supply current $\hat{i}$ is taken as constant and the current curve as symmetrical starting from the center point. This yields Eq. 13:

$$E_{max}(r) \approx \frac{Z_0 \cdot \hat{i}}{2 \cdot \pi \cdot r}, \tag{13}$$

with $r = 3$ m and $\hat{i} = 1$ A following a maximum field strength of 20 V/m. As can be seen, it is frequency-independent since the equation is valid for the resonance case with $l = \lambda/2$. The results of the verification can be seen in Figure 8A. In a range from 100 MHz to 1 GHz 10, operating points are shown as proof. The electric far fields are given by calculation and verification. Here, a good agreement with deviations of less than 0.9% is shown (Figure 8B). The maximum deviation of 0.9% is taken as the error limit for the results in the next chapter. The higher the frequency, the better the match since *CST* calculates to a distance of $r = 3$ m. The consideration $l \ll r$ therefore becomes better.

The remaining deviations can be described as follows: The derivation assumes perfect verification models and is implemented in the verification where possible. For example, a gap exists between both dipole ends, and the wires have a finitely small radius. Furthermore, the most ideal boundary conditions are assumed, where, in the verification, limits are reached due to computationally intensive processes. In addition, in the verification, the source itself is already radiating, which is unavoidable. Due to these explainable limitations and effects, the verification represents a good match with the calculation. Based on this good agreement, the verification model, including schematic and especially the simulation environment, is trusted.

6 Results

The results of the simulation are presented as follows. To identify possible ion beam configurations and their impact on the electric far field, several simulations were performed, and one parameter was changed in each case (Table 1). The RIT is briefly explained to better understand the simulation parameters. Generally, the RFG provides energy to the thruster coil; it thus controls the operating point of the thruster, which makes it a crucial part of the RIT assembly. A RIT consists of a coil wound around a vessel, where a plasma is generated. With a grid structure at this vessel to the outside, the ions will be accelerated and extracted to generate thrust. There is an electric field between the grids because a high voltage is connected from the outside. The RFG is operated at different voltages of the full bridge as well as frequencies, depending on the operating points. For the ion beam, the parameters' divergence angle, beam current, and grid voltage are changed. The last two parameters contribute directly to the conductivity (Eqs. 4, 5). For all simulations, the distance of the far-field measurement is 3 m.

First, the simulation with and without the ion beam is investigated. This determines the general importance of the research. Without a decisive difference, further investigation of the ion beam would not be important as no significant degradation on the EMC has occurred.

The emissions in the far field are shown in Figure 9 for simulation #5 with and without the ion beam at different frequencies. It is qualitatively evident that the ion beam has a considerable influence on the overall emission characteristics of strength and shape, increasing the emission values and the relevant radiation range. A diagram with concrete electric field strengths is shown in Figure 10A, where the ion beam provides a significant increase in electric field strength in the far field. This increase is explained, on the one hand, by the newly established antenna effect due to the conductive ion beam. In addition, the ion beam conducts more effective emissions out of the thruster housing because it is directly connected to the plasma inside. The emissions in the high-frequency range are generated by the feed signal of the full bridge of the RFG. It is a square wave signal, which contains high-frequency components due to the sharp rising and falling edges.

We now consider the individual changes of the ion beam properties. Figure 10B shows all five configurations; the legend numbers refer to those in Table 1. In general, it can be seen that the progressions of the emission curves are the same: there are

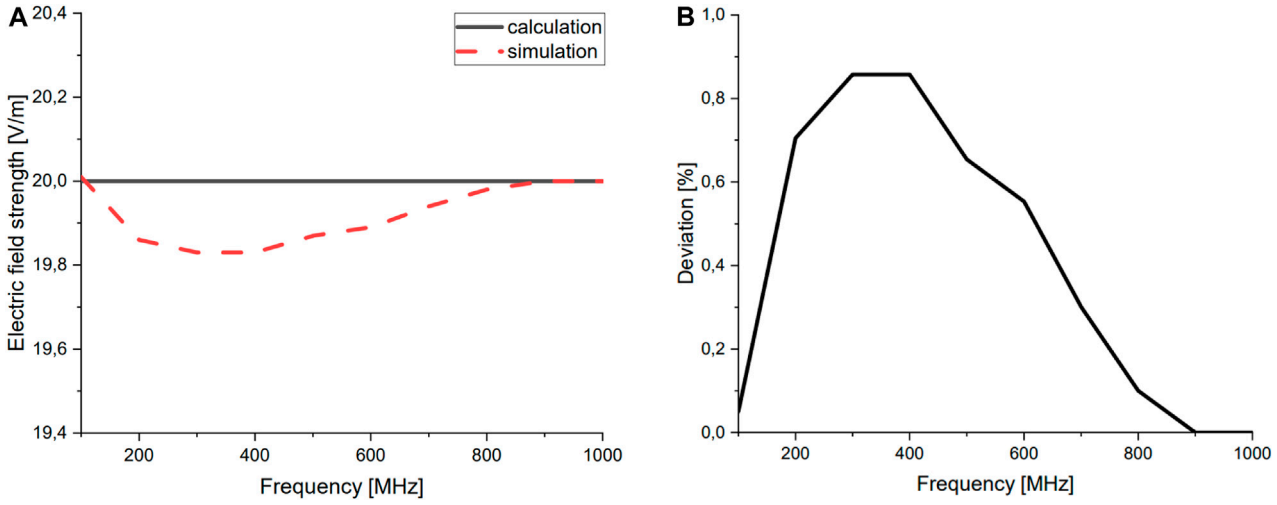

FIGURE 8
(A) Electric field strengths in *V*/*m* calculated on the basis of a Hertzian dipole in $r = 3$ m distance, **(B)** % deviation between verification and calculation.

TABLE 1 Simulation characteristics.

#	Control signal	Ion beam	Measurement(m)
1	±5.5 V, 3.05 MHz	10 deg div angle, 10 mA beam current, 1 kV grid voltage	3
2	±12 V, 3.05 MHz	10 deg div angle, 10 mA beam current, 1 kV grid voltage	3
3	±5.5 V, 3.05 MHz	3 deg div angle, 10 mA beam current, 1 kV grid voltage	3
4	±5.5 V, 1 MHz	10 deg div angle, 10 mA beam current, 1 kV grid voltage	3
5	±5.5 V, 3.05 MHz	10 deg div angle, 50 mA beam current, 2 kV grid voltage	3

isolated spikes at different frequencies, and the level of emissions varies, which will be discussed in more detail below: A higher voltage of the RFG output, and thus a higher power input to the thruster coil, ensures higher emissions. At frequencies above 500 MHz, the electric field strength is similar. At a voltage of 5.5 V, an amplitude of 1.3 A is achieved; at 12 V, it is 2.8 A. A smaller divergence angle has a positive effect on the emission characteristics of the thruster. In the lower frequency range, a reduction from 10° to 3° provides an emission optimization of up to 20 dB, which corresponds to a factor of 10. As the frequency increases, this gap becomes smaller and is reduced to about 10 dB (factor of 3). When the frequency of the drive signal is reduced from 3.05 MHz to 1 MHz, the field strength is increased in the lower frequency range up to 300 MHz. In the further course, the emissions of both frequencies almost coincide. In simulation #5, the ion beam has a higher conductivity, which causes the emissions to drop sharply. The graph is comparable to that from simulation #3. The same deviations from the reference from simulation #1 are achieved.

To further characterize the results, significant resonance locations are now discussed. Resonances *P*1 and *P*2 (Figure 10A) are due to the thruster geometry—more specifically, the extraction grids. Previous research shows that resonances in this high-frequency range are roughly proportional to the size of the extraction grid (Baruth, 2017). The simulation confirms this as resonance also occurs with and without the ion beam. The resonance *P*3 (Figure 10B) is shifted due to the changed frequency of the drive signal (simulation characteristic #3) but can still be assigned to the grid geometry.

In summary, more injected power and a larger divergence angle of the beam mean higher emissions. If the conductivity of the beam is increased or if the divergence angle is decreased, the emission of the thruster assembly is reduced. The parameters of the ion beam provide the characteristics of the radiation. To generate low radiation, it is necessary to adjust these parameters depending on the possibilities. Varying the frequency of the excitation signal makes a difference, but it is not as crucial as changing the direct parameters of the ion beam.

7 Discussion

The simulation was thus successfully established. The RIT-4 model was supplemented with the ion beam replica and examined. The ion beam has a high influence on the emission characteristics of the thruster assembly. Likewise, the properties of the ion beam play a major role; depending on the design, more or fewer emissions can be expected and quantitatively predicted with acceptable accuracy. These studies contribute to the expansion of science because new

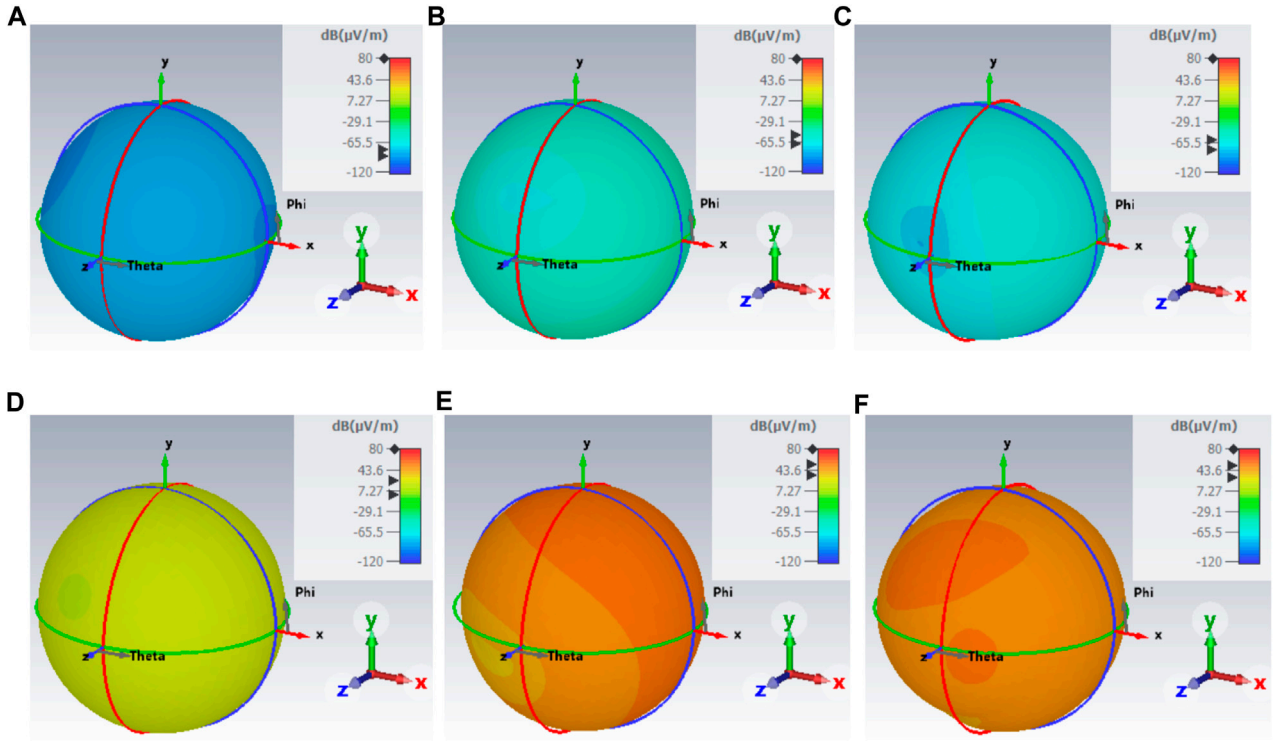

FIGURE 9
3D electric far field in 3 m distance for simulation #5: **(A)** without ion beam at *f* =101 MHz, **(B)** without ion beam at *f* =505 MHz, **(C)** without ion beam at *f* =1 GHz, **(D)** with ion beam at *f* =101 MHz, **(E)** with ion beam at *f* =505 MHz, and **(F)** with ion beam at *f* =1 GHz.

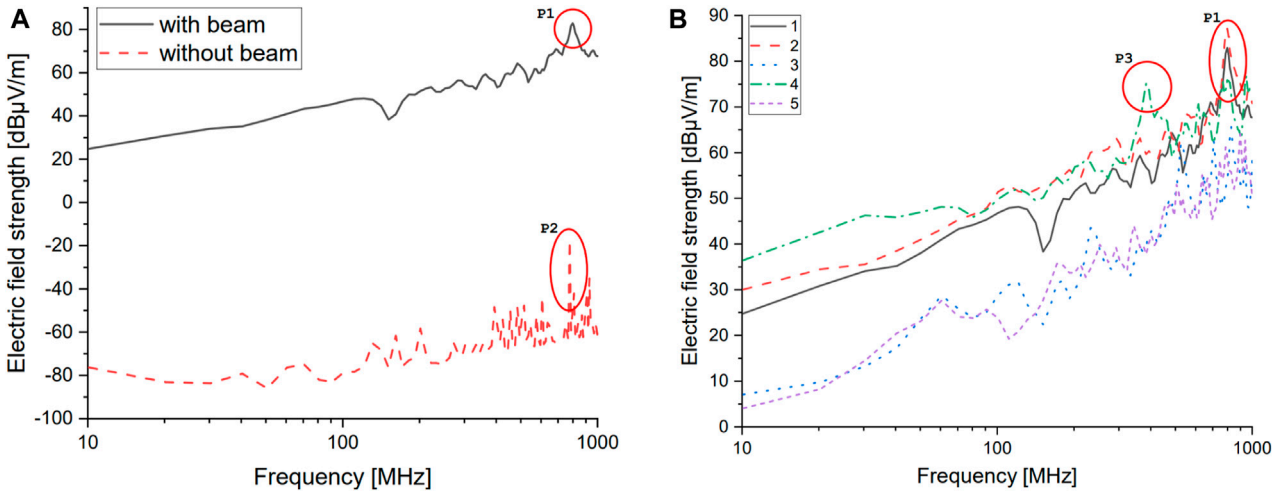

FIGURE 10
Electric far field in 3 m distance: **(A)** simulation #1 with and without ion beam; **(B)** all simulation variants.

insights are gained into the emission characteristics of the thruster. Furthermore, by entering the thruster parameters as well as the operating point, it is possible to discover the emissions of the thruster and ion beam combination.

The next steps are to embed this knowledge into the overall system. Elaborations exist on the RFG, the thruster itself, and the corresponding cabling. The insertion of a neutralizer with electron emission is planned for future research. These results will be combined to lead to a holistic EMC system. Further measurements need to be made with the EMC vacuum chamber that include comparable setups. If these two procedures match, a good prediction can be made with the help of the simulation, which provides information about EMC behavior even before the development of the thruster assembly. This results in shorter test

times and less post-development. Furthermore, other EMC areas such as near-field can be analyzed in future research. Moreover, the possibility of extending the model to other ion thrusters, such as a Hall effect thruster, and predicting their ion thruster behavior should be explored.

Data availability statement

The raw data supporting the conclusion of this article will be made available by the authors without undue reservation.

Author contributions

YR: conceptualization, data curation, formal analysis, investigation, methodology, resources, software, validation, visualization, writing–original draft, and writing–review and editing. RT: writing–review and editing, and methodology. UP: funding acquisition, project administration, and writing–review and editing. CV: methodology, project administration, supervision, validation, and writing–review and editing.

Funding

The authors declare that financial support was received for the research, authorship, and/or publication of this article. This work was financially supported by the German Federal Ministry of Education and Research, grant number 13FH173PX8.

Acknowledgments

This publication represents a component of the corresponding author's doctoral thesis in the Department of Physics at the Justus-Liebig-University Giessen, Germany, in cooperation with Technische Hochschule Mittelhessen—University of Applied Sciences at the Graduate Centre of Engineering Sciences at the Research Campus of Central Hessen.

Conflict of interest

The authors declare that the research was conducted in the absence of any commercial or financial relationships that could be construed as a potential conflict of interest.

Publisher's note

All claims expressed in this article are solely those of the authors and do not necessarily represent those of their affiliated organizations, or those of the publisher, the editors, and the reviewers. Any product that may be evaluated in this article, or claim that may be made by its manufacturer, is not guaranteed or endorsed by the publisher.

References

Baruth, T. (2017). *Analysis on the electromagnetic compatibility of radio-frequency ion thrusters using a RIT4*. Giessen, Germany: University of Giessen. Available at: http://geb.uni-giessen.de/geb/volltexte/2017/12495/.

Becker, R., and Herrmannsfeldt, W. B. (1992). i g u n–A program for the simulation of positive ion extraction including magnetic fields. *Rev. Sci. Instrum.* 63, 2756–2758. doi:10.1063/1.1142795

Chabert, P., and Braithwaite, N. (2011). *Physics of radio-frequency plasmas*. 1. Cambridge: Cambridge University Press. ISBN 978–0–521–76300–4.

Dobkevicius, M., and Feili, D. (2016). A coupled performance and thermal model for radio-frequency gridded ion thrusters. *Eur. Phys. J. D.* 70, 227. doi:10.1140/epjd/e2016-70273-7

European cooperation for space standardization (2012). *ECSS-E-ST-20-07C rev. 1*. Noordwijk (Netherlands): ESA-ESTEC Requirements and Standards Division.

Goebel, D. M., and Katz, I. (2008). *Fundamentals of electric propulsion: ion and Hall thrusters*. New Jersey, United States: Wiley. ISBN 978-0-470-42927-3.

Gustrau, F. (2015). *Elektromagnetische verträglichkeit*. Munich, Germany: Hanser. ISBN 978-3-446-44301-3.

Holste, K., Dietz, P., Scharmann, S., Keil, K., Henning, T., Zschätzsch, D., et al. (2020). Ion thrusters for electric propulsion: scientific issues developing a niche technology into a game changer. *Rev. Sci. Instrum.* 91, 061101. doi:10.1063/5.0010134

International Electrotechnical Commission (2018). *IEC standard 60050-161-01-07: international electrotechnical vocabulary: electromagnetic compatibility: basic concepts*.

Jackson, J. D. (1998). *Classical electrodynamics*. 3. New Jersey, United States: Wiley. ISBN 978-0-471-30932-1.

Kalvas, T., Tarvainen, O., Ropponen, T., Steczkiewicz, O., Ärje, J., and Clark, H. (2010). IBSIMU: a three-dimensional simulation software for charged particle optics. *Rev. Sci. Instrum.* 81, 02B703. doi:10.1063/1.3258608

Kark, K. W. (2016). *Antennen und Strahlungsfelder*. 6. Cham: Springer Vieweg. ISBN 978-3-658-13965-0 (eBook).

Reeh, A., Probst, U., and Klar, P. J. (2017). "3D ion extraction code incorporated self-consistently into a numerical model of a radio-frequency ion thruster," in 35th International Electric Propulsion Conference, Daniłko, Dariusz, October 8 – 12, 2017. Atlanta, Georgia (US), IEPC-2017-326.

Reeh, A., Probst, U., and Klar, P. J. (2019). Global model of a radio-frequency ion thruster based on a holistic treatment of electron and ion density profiles. *Eur. Phys. J. D.* 73, 232. doi:10.1140/epjd/e2019-100002-3

Reynolds, T. W. (1971). *Mathematical representation of current density profiles from ion thrusters*. Cleveland, Ohio: NASA Lewis Research Center. Technical Report NASA TN-D6334.

Rover, Y., Thüringer, R., Volkmar, C., Probst, U., Kiefer, F., Holste, K., et al. (2023). Semi-anechoic chamber for electromagnetic compatibility tests of electric propulsion thrusters. *J. Electr. Propuls.* 2, 3. doi:10.1007/s44205-023-00039-w

Rover, Y., and Volkmar, C. (2022). "Verification of a radio-frequency generator model in a full-wave 3D EM simulation," in *IEEE aerospace conference* (Montana (US): Big Sky). 978-1-6654-3760-8/22/$31.00.

Scholze, F., Bundesmann, C., Eichhorn, C., and Spemann, D. (2019). "Determination of the beam divergence of a gridded ion thruster using the AEPD platform," in 36th International Electric Propulsion Conference, Vienna, Austria, September 15-20, 2019. IEPC-2019-A-738.

Symeonidis, S. (2018). *CST-MATLAB-API*. v1.0.0. doi:10.5281/zenodo.1237969

Zhang, H., Zhang, Y., Huang, C., Yuan, Y., and Cheng, L. (2021). *Spacecraft electromagnetic compatibilities Technologies*. Cham: Springer. ISBN 978-981-15-4781-2. doi:10.1007/978-981-15-4782-9

3.3 Dritte Veröffentlichung

Semi-anechoic chamber for electromagnetic compatibility tests of electric propulsion thrusters

Yannik Rover, Rainer Thüringer, Chris Volkmar, Uwe Probst, Felix Kiefer, Kristof Holste und Peter J. Klar

©2023. Reprinted, with permission, from Y. Rover, R. Thüringer, C. Volkmar, U. Probst, F. Kiefer, K. Holste and P. J. Klar, "Semi-anechoic chamber for electromagnetic compatibility tests of electric propulsion thrusters", J Electr Propuls 2, 3 (2023), https://doi.org/10.1007/s44205-023-00039-w; Creative Commons Attribution 4.0 International License: https://creativecommons.org/licenses/by/4.0/, no changes made.

Autorenbeiträge

Felix Kiefer und der korrespondierende Autor Yannik Rover waren an der Einrichtung der Kammer beteiligt und führten die ersten Messungen sowie die Auswertung der Rohdaten durch. Yannik Rover verfasste den Entwurf des Manuskripts und alle Autoren kommentierten frühere Versionen des Manuskripts. Alle Autoren lasen und genehmigten das endgültige Manuskript.

Einordnung in das Gesamtvorhaben

Eine halb-reflexionsfreie Absorberkammer enstand ausgehend von dem Stand der Wissenschaft. Dieses Vorhaben ist in der Veröffentlichung dargestellt. Der Vorteil dieser Testeinrichtung im Gegensatz zu bestehenden Anlagen ist die zusätzliche Schirmung an der Verbindungsstelle von Absorberraum und Vakuumtank, wodurch externe elektromagnetische Störungen eliminiert werden. Des Weiteren ist ein Wabenkamin verbaut. Dieses Element ist gasdurchlässig, aber EMV-dicht, sodass Störsignale durch Anbauteile, wie Pumpen, an Flanschen nicht bis in den Messbereich gelangen [**Thu19**].

Rover *et al. Journal of Electric Propulsion* (2023) 2:3
https://doi.org/10.1007/s44205-023-00039-w

Journal of Electric Propulsion

RESEARCH Open Access

Semi-anechoic chamber for electromagnetic compatibility tests of electric propulsion thrusters

Yannik Rover[1*], Rainer Thüringer[1], Chris Volkmar[1], Uwe Probst[1], Felix Kiefer[2], Kristof Holste[2] and Peter J. Klar[2]

*Correspondence:
yannik.rover@nanop.thm.de

[1] Center of Competence for Nanotechnology and Photonics (NanoP), TH Mittelhessen University of Applied Sciences, Wiesenstrasse 14, Giessen 35390, Hesse, Germany
[2] Institute of Experimental Physics I, University of Giessen, Heinrich-Buff-Ring 16, Giessen 35392, Hesse, Germany

Abstract

The present work deals with electromagnetic compatibility (EMC) investigations in the field of electric propulsion (EP). A semi-anechoic chamber (SAC) was set up to perform EMC tests with thrusters under operating conditions. The facility includes a semi-anechoic room and a vacuum tank. The measurement electronics currently have an upper frequency limit at 18 GHz. Initial measurements were done operating a Pulsed Plasma Thruster (PPT) to familiarize with the electronic systems. The same device under test (DUT) was investigated in a reverberation chamber (RVC) to obtain comparative results which showed good agreement. Furthermore, the anechoic chamber shows satisfactory initial measurement characteristics, which will be further tested and improved in the future. Characteristics such as chamber pressure, base noise show realistic values. The next steps are to perform measurements on radio-frequency ion thrusters (RIT) including peripherals and cabling.

Keywords: Electric propulsion, Electromagnetic compatibility, Semi-anechoic chamber, Radiation

Introduction

Nowadays, electric thrusters are important propulsion systems in space. Increasing commercialization has a major impact on space flight and especially on electric propulsion. Strong reasons for emerging space travel are scientific, political, military and economic objectives. The still existing challenges are leading to extensive research in energy efficiency, electromagnetic compatibility, alternative propellants, and scalability, to name a few [1]. Electromagnetic compatibility is "the ability of an equipment or system to function satisfactorily in its electromagnetic environment without introducing intolerable electromagnetic disturbances to anything in that environment", as defined in [2]. EMC technology for spacecraft is based on traditional theory, but the situation is further complicated by requirements on weight, reliability, space environment, and cost. For this reasons, the commonly used ferrite absorbers or an additional shielding may not be the first choice. Therefore, design methods should focus on bonding, grounding, routing and cable layout. Since spacecraft are typically subject to various operating conditions, e.g., integration testing, launch, and on-orbit operation, special attention should

Springer

© The Author(s) 2023. **Open Access** This article is licensed under a Creative Commons Attribution 4.0 International License, which permits use, sharing, adaptation, distribution and reproduction in any medium or format, as long as you give appropriate credit to the original author(s) and the source, provide a link to the Creative Commons licence, and indicate if changes were made. The images or other third party material in this article are included in the article's Creative Commons licence, unless indicated otherwise in a credit line to the material. If material is not included in the article's Creative Commons licence and your intended use is not permitted by statutory regulation or exceeds the permitted use, you will need to obtain permission directly from the copyright holder. To view a copy of this licence, visit http://creativecommons.org/licenses/by/4.0/.

be paid to the effects of these conditions on the electromagnetic environment (EME). Hence, the EMC characteristics of the spacecraft are associated to its EME [3]. To meet these requirements, a vacuum EMC test facility is used. In past studies some parts of the thruster assembly have been studied separately, e.g., a radio-frequency generator was investigated for its EMC by simulation and measurement. It became clear that the supply lines and the cabling to the thruster are the decisive influencing factors from an EMC point of view [4]. Furthermore, a honeycomb was designed in a previous research work. This is located in the vacuum tank and ensures the absorption of electromagnetic interference from outside [5]. With these basics, the holistic view of the assembly will now be carried out with the help of the SAC.

The latest searches show that there are only a few such facilities in the world. Moreover, the facility considered here is the only one in the university environment. Another test facility is located in California at the company "The Aerospace Corporation". The basic design is the same as the one presented here [6]. The "Research Institute of Applied Mechanics and Electrodynamics of the Moscow Aviation Institute (RIAME MAI)" also has an identical facility [7]. Zhang et al. also describe an EMC test facility. There is no indication of where this facility is located [3]. The design of the facilities presented is consistent with the design of this facility. The honeycomb chimney is a proprietary development that is not used elsewhere. However, this setup is crucial because it ensures trouble-free operation of the vacuum chamber. The honeycomb chimney is gas-permeable but EMC-tight.

The device under test is a pulsed plasma thruster. The PPT was designed by the Institute of Space Systems (IRS) at the University of Stuttgart for the CubeSat GreenCube and is called PETRUS 1J. The propulsion module contains a group of four PETRUS pulsed plasma thrusters with a common 1 joule capacitor bank. As a fully integrated system, this DUT does not require a complex external power supply system, apart from a voltage source and two communication cables. The charging voltage of the capacitor bank is 5 volts [8].

The main goal of the ongoing research is the completion of the vacuum EMC chamber and the proper operation of the measurement equipment. Furthermore, the matches of the reverberation chamber and absorber chamber are to be worked out. Possible differences are to be explained. The radiation characteristics of the PPT are to be verified, both chambers are necessary for this purpose.

The motivation of this work is presented in Section Motivation. Section Facility design describes the structure and components of the test facility. Additional features are shown in Section Facility features. Section Comparison: Reverberation chamber compares the test facility with another facility using a different physical principle. Initial measurements are shown in Section Measurement, including various operating points of the thruster. Finally, in Section Conclusion, a summary of the work and its outputs is given, along with an outlook.

Motivation

Ion thrusters, which constitute an essential part of "NewSpace" missions, play a major role in spacecraft systems for propulsion and maneuvering. Therefore, the thrusters and their peripherals must be safe and reliable. In addition to functionality, electromagnetic

compatibility requirements must also be met to always ensure stable operation under all operating conditions. Furthermore, the mutual interference of active high-frequency components - such as the radio-frequency generator typically used with RF ion thrusters - and satellite components regarding immunity and emissions must be considered. In fact, the electronics constitute about 60 % of the total thruster assembly, which shows the importance of examinations of those allegedly "peripheral" components and their interaction with the thruster itself and other satellite components.

Facility design

The vacuum EMC test facility consists of two parts. Figure 1 shows a schematic representation. The first part, a semi-anechoic chamber, describes a defined environment for EMC testing. In general, it is a room consisting of a metallic, electrically conductive housing in which EM fields are decoupled from the outside. In addition, the walls and ceiling are covered with absorber material to eliminate reflections and thus mimic far field conditions. There are two panels in the floor to connect the DUT to all necessary cabling and further supply lines from the outside. There are also two panels in the wall to supply the anechoic room with gas for the thruster and water for cooling systems. Another important aperture is the feedthrough to the vacuum vessel. It is made with a GRP (glass-fibre reinforced plastic) cyclinder with an epoxy resin. The wall thickness is about 21 mm. On both sides of the wall is still a UV protective layer. A metal flange connects the GRP cylinder and vacuum tank. The material has the advantage of being transparent to electromagnetic radiation to a certain extent. The transparency function as well as the influence of the metal flange are subject to an ongoing investigation. This characteristic allows to perform radiation and susceptibility measurements. The vacuum vessel is shown in Fig. 2. It contains a beam dump, a honey comb and several openings for pumps, feedthroughs and sensors. The honey comb was previously researched and laid out as described in [5]. Simulations resulted in a damping of the radiation with more than 100 dB using long honey comb chimneys. The pumping system consists of a backing pump, a turbomolecular pump and a cryopanel which are located adjacent to the tank. The backing pump is a "Leybold DRYVAC DV 200" with a nominal pumping speed of 210 m^3/h and an ultimate pressure of 0.01 mbar. The turbomolecular pump is

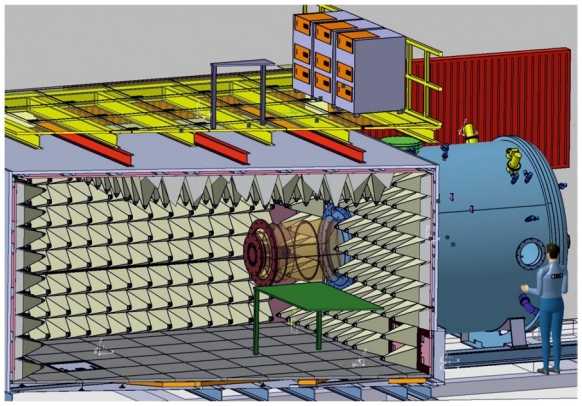

Fig. 1 Conceptual drawing of the vacuum EMC test facility: Semi-anechoic room (left) and vaccum vessel (right)

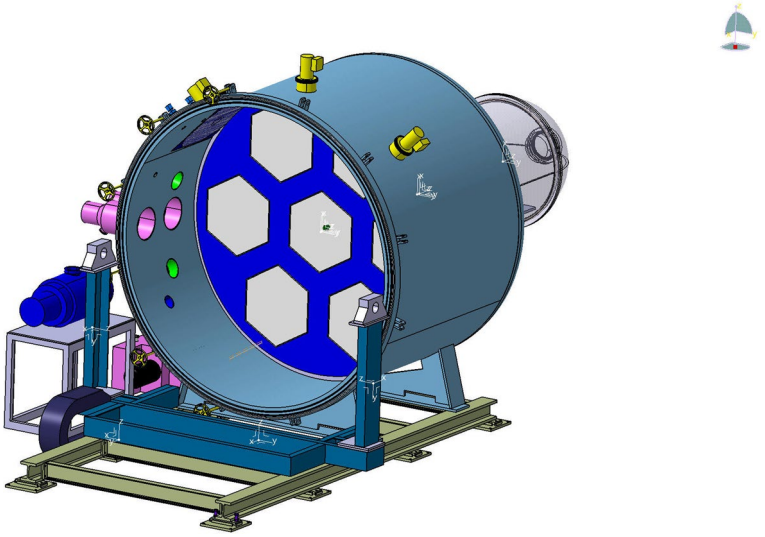

Fig. 2 Conceptual drawing of vacuum vessel: GRP cylinder, beam dump and honey comb

a "Edwards STP-iXA4506C" with a rated speed of 24200 rpm or 3000 l/s The thruster is mounted inside the GRP cylinder. A beam dump is used to absorb particle energy. Behind it is a honey comb that ensures that the vacuum area of the facility is completely free of radiation from the outside, caused by vacuum pumps, gauges and other feedthroughs. Thus, the entire pumping system is located in an EMC-tight but gas-permeable second part of the vacuum vessel. A general measurement setup includes a DUT, an antenna and measurement electronics. The DUT consists of a thruster and its peripheral devices, e.g. in case of a RIT: a radio-frequency generator and high voltage power supplies for the grids. The measurement electronics include the signal generators and amplifiers for susceptibility tests and analyzers for radiation testing.

The measurement electronics is formed by Rohde & Schwarz systems. The measuring procedure is controlled and evaluated by the software EMC32 version 11.40.00. The signal generator is a "Rohde & Schwarz SMB 100A" with a frequency range of 100 kHz to 20 GHz. The hardware control unit is a "Rohde & Schwarz OSP220" model, this is used to switch various signal paths on or off, depending on the hardware configuration and test setup. The spectrum analyzer is a "Rohde & Schwarz ESW26" with a frequency range up to 26.5 GHz. The used antenna is a "Schwarzbeck VULB 9162" with a frequency range of 25 MHz to 8 GHz.

Facility features

The anechoic room is 5.5 m long and 4.8 m wide. The height ist about 3.2 m. It is designed for a frequency range from 30 MHz to 40 GHz. Emission and immunity tests comply with MIL and ECSS standards. The standard distance between the antenna and DUT is specified as 1 m. The vacuum vessel has a diameter of 2.75 m. The current configuration of the electronic equipment is divided into emission and susceptibility tests. Furthermore, a distinction is made between conducted and radiated investigations. Thus, there are four testing conditions: conducted emissions (CE), radiated emissions (RE), conducted susceptibility (CS) and radiated susceptibility (RS). The following Table 1

Table 1 EMC measurement options and ranges

CE (differential-mode)	30 Hz to 100 MHz
CE (common-mode)	100 kHz to 100 MHz
RE (low frequency)	electric and magnetic field
RE (electric field)	30 MHz to 18 GHz
CS (differential-mode)	30 Hz to 100 kHz
CS (common-mode)	50 kHz to 100 MHz
RS (magnetic field)	30 Hz to 100 kHz
RS (electric field)	30 MHz to 18 GHz

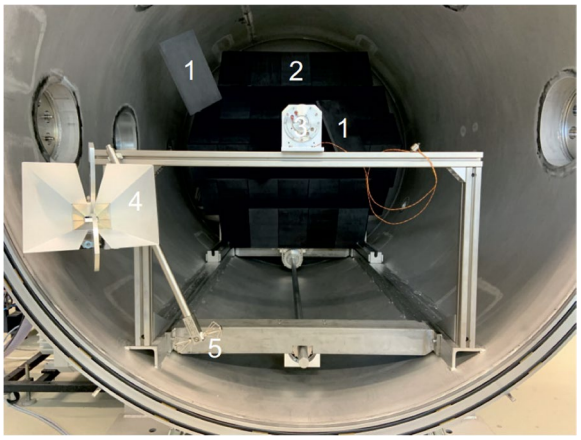

Fig. 3 Reverberation chamber at Justus-Liebig-University: (1) mode stirrer, (2) beam dump, (3) thruster, (4) and (5) measurement antennas

shows the frequency ranges for each measurement option. Currently, the limitation in frequency is 18 GHz. An upgrade from 18 GHz to 40 GHz is planned.

There are also some limitations, which are issues in an ongoing research, that must be considered when using thrusters. The size of the thruster under investigation depends on the divergence angle of the ion beam, due to the nature of the vacuum vessel. Finally, the ion beam should not hit the walls of the tank, but the beam dump. Initial approaches indicate that a size of RIT-10 to RIT-15 from the manufacturer ArianeGroup is possible. For more information about the RIT properties, see [1]. Furthermore, it will be investigated whether CubeSat systems can also be completely measured. Another influence is the limitation by thermal management, especially for endurance tests. Due to the pumping speed of the pumps, a gas flow of 50 sccm should be possible.

Comparison: Reverberation chamber

Another facility for diagnosing EMC characteristics is a reverberation chamber (see Fig. 3), which is also operated at Justus-Liebig-University in Giessen. The chamber is 1.6 m in diameter and approximately 2.4 m long. The dedicated pumping system consists of two backing pumps and a turbomolecular pump and reaches an initial pressure of less than 10^{-6} mbar, which increases to about $3 \cdot 10^{-6}$ mbar when $q = 0.25$ sccm Xe propellant flows into the chamber. The laboratory is air-conditioned to minimize the temperature effects on the equipment and the feed system. The vacuum chamber has a graphite

beam dump, which collects the ejected ion plume [9]. The purpose of this concept is to investigate the applicability of a reverberation vacuum chamber in the field of electric propulsion. The DUT and other peripherals to be investigated are operated in the chamber. The RVC is based on the principle of a cavity resonator, where usually only discrete modes propagate, which means that discrete frequencies can be observed at high field strength, while medium frequencies are strongly attenuated. To obtain a continuous frequency spectrum, at least one rotating metal stirrer is used, which changes the EM boundary conditions depending on its angular position. A time-varying mode spectrum is measured with the introduced measurement equipment and an antenna with a frequency range from 500 MHz to 18 GHz. Measurements in the reverberation chamber are possible at frequencies above the cut-off-frequency. It is defined by the geometry of the metallic vessel and is determined experimentally during commissioning of the chamber. The cut-off frequency can be interpreted in different ways. On the one hand as the first fundamental mode (theoretically calculable according to Weyl's formula [10]) or as soon as enough modes have propagated in the chamber, a kind of stability criterion. The first fundamental mode was calculated to 378 MHz. For more information about the characteristics and especially the preceding simulation model, see [9]. However, since the beam dump and other components such as the antenna and thruster reduce the volume of the chamber, the resonant frequency increases slightly.

The main difference to the semi-anechoic chamber is that very high field strengths can be generated with a comparatively low feed-in power. Whereas the semi-anechoic chamber is a replica of the free space [11].

Measurement

Initial measurements were conducted with the PPT to test the operation of the devices and check the electromagnetic characteristics. Furthermore, a cross-check with the reverberation chamber was performed. As can be seen in Fig. 4, the PPT is located inside the GRP cylinder, only its electrical connections are routed out of the chamber to supply the thruster. The thruster system consists of the four PETRUS PPT and a black box containing a communication and control module. Also included is a charge and ignition unit. The cabling consists of the power supply lines, two communication

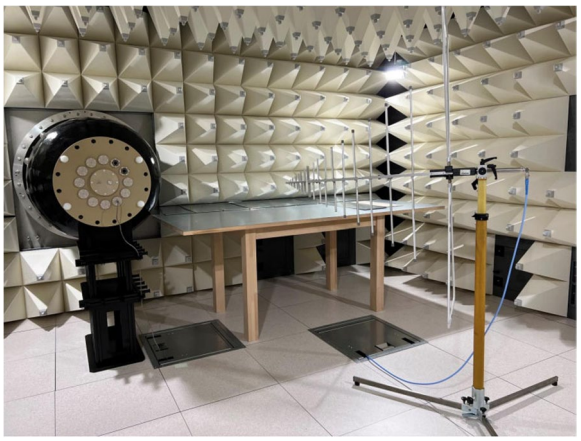

Fig. 4 Measurement setup with PPT inside GRP cylinder and antenna

cables and a ground cable. The PPT module is grounded to the semi-anechoic chamber. The mounting of the PPT is not grounded. The initial pressure of the SAC is below 10^{-6} mbar, which increases to about $7 \cdot 10^{-6}$ mbar at $q = 0.25$ sccm Xe propellant flow. The thruster is operated nominally. The PPT burns its on-board solid propellant, and the pulsed extractions here occur at 2 Hz. PPT with solid propellant have a negligible effect on the background pressure of the chamber compared to systems with gas flow such as an RIT. The temperature was not determined before, during or after the measurement.

Since the PPT is ignited at 2 Hz, this corresponds to a pulse length of 500 ms. Accordingly, the spectrum analyzer is triggered every 500 ms to sample a frequency range. This ensures that a pulse of the PPT takes place in each frequency range. The measurement therefore starts at 30 MHz and runs step by step through the frequency range up to 8 GHz, with a dwell time of 500 ms per frequency window, the step size is logarithmic, otherwise the measurement would be too time-consuming. Before starting operation and measurement, a steady state of the chamber pressure was waited for.

As shown in Fig. 5, the results include the noise caused by ambient radiation and the radiation caused by the PPT. For comparison, the results in both the semi-anechoic chamber and the reverberation chamber are shown. In the reverberation chamber, the lowest useable frequency is about 300 MHz due to the available antennas. In any case, the results in the reverberation chamber are only meaningful above 378 MHz, which is approximately the stable cut-off-frequency of the cavity. The antenna in the semi-anechoic chamber has its highest frequency at 8 GHz.

The discrepancy between the SAC and RVC results can be explained as follows: First, the background radiation between SAC and RVC facilities is different due to different methods of calculating the field strength. The lower characteristic curve of the RVC facility means that it is more sensitive compared to the SAC facility. The increased sensitivity can be recognized by the base noise, which is significantly lower in the RVC. This makes it possible to detect lower field strengths. In the reverberation chamber, the total power of the DUT is obtained by the antenna, which is increased by the amplification of cavity resonators. The energy radiated above the cutoff frequency is reflected several times in the RVC and can be damped to a lesser extent compared to the SAC setup.

In the EMC32 software module for the RVC, the antenna distance is set to 1 m, since the standards require such a distance. Since no such distance can be maintained in the

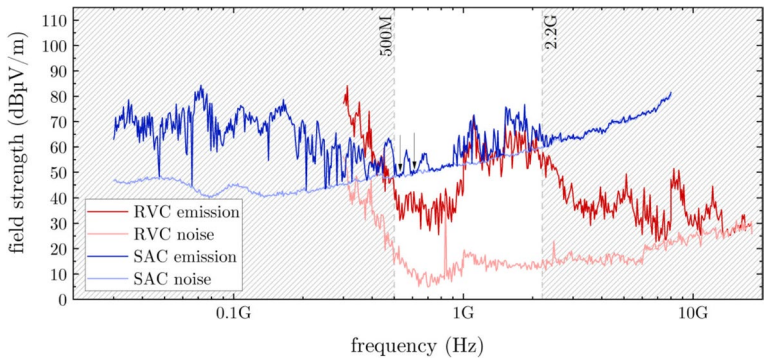

Fig. 5 Measurement results with comparison of reverberation chamber. SAC noise (light blue), PPT in SAC (blue), RVC noise (light red), PPT in RVC (red)

chamber, the measurement distances in the RVC are only virtual and therefore calculated. In the SAC, however, the distance 1.5 m was used due to calibration data of the antenna. The resulting deviation was compensated by the free space attenuation. Its calculation is done with Eqs. (1) and (2) [12]:

$$F = \left(\frac{4 \cdot \pi \cdot r}{\lambda}\right)^2 \tag{1}$$

$$F_{\mathrm{dB}} = 10 \cdot \log_{10}(F) \tag{2}$$

where r is the distance between antenna and DUT, λ is the wavelength. To give an example for a frequency of approximately 1.1 GHz, the emissions are 74 dBµV/m (SAC) and 100 dBµV/m (RVC). The difference is about 26 dB and the free space attenuation is calculated to 27.25 dB. This calculation is performed over the entire frequency range and is already considered in Fig. 5. For a good overview, the background noise has been subtracted from the thrusters emissions and can be seen in Fig. 6. Comparing both plots, the SAC emissions are slightly higher than the RVC's, which is a good correlation for these measurements. Since the system is a SAC, there are no absorbers mounted on the floor. Ground reflections occur, and the conditions of free space are accordingly not quite met. This creates further interference paths to the receiving antenna, depending on its position and the wavelength. Furthermore, the GRP cylinder has not yet been conclusively investigated; currently, no attenuation or even amplification due to multipath propagation is assumed. A frequency-dependent detection is required for this. Accordingly, existing deviations will be examined more closely in the next steps.

Conclusion

In summary, the facility has been built and the measurement equipment has been set up. First measurements on the ambient radiation and a PPT were performed and compared with the results in the reverberation chamber. Due to the lack of reference values, little can be said about the quality of the PPT from an EMC point of view. The radiation

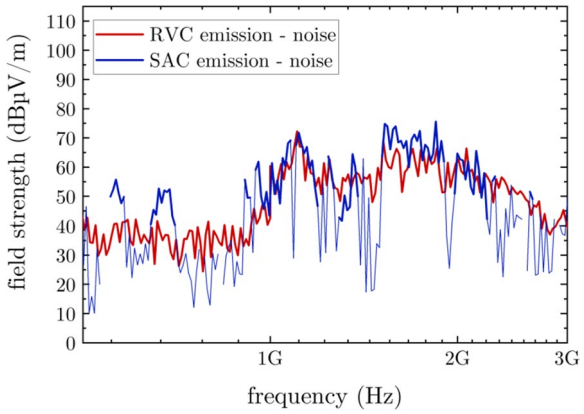

Fig. 6 SAC measurement results compared to RVC results. The ambient radiation is subtracted from the PPT data with signal-noise-ratio (SNR) > 110 % (bold lines) and SNR ≤ 110 % (narrow lines). PPT in SAC (blue), PPT in RVC (red)

pattern of the PPT is verified, due to the high agreement of the measurements in both chambers. Due to the mutual comparison of the measured values, both chambers agree and can be used. The research carried out contributes to the expansion of science insofar as new knowledge about the functionality of the chambers has been gained. Most important is the realization that the reverberation chamber can also be used for EMC measurements in the field of electric propulsion.

To give an outlook, the next steps are to eliminate the discrepancies between SAC and RVC and to perform further tests to see if both chambers can be considered equivalent. The damping/strengthening of the GRP cylinder and also the damping determination of the honeycomb are part of the future activities. When consistent and traceable results are available, the following work is planned: Comparison of two RIT and the inclusion of peripherals. The influence of wiring and its routing are also important for EMC testing for thruster assemblies. The influence and detection of thermal characteristics is also an important research topic. Depending on the dependence of the possible sizes and powers of the thrusters, tests with total systems such as CubeSats are also planned.

Acknowledgements
This publication represents a component of the corresponding author's doctoral thesis in the Department of Physics at the Justus-Liebig-University Giessen, Germany in cooperation with Technische Hochschule Mittelhessen - University of Applied Sciences at the Graduate Centre of Engineering Sciences at the Research Campus of Central Hessen. Special thanks go to F. Schaefer from the Institute of Space Systems (IRS) at the University of Stuttgart for providing the EUT and authorizing the publication of the measurement data.

Authors' contributions
Corresponding author Yannik Rover and Felix Kiefer were involved in the setup of the chamber and performed the initial measurements as well as the evaluation of the raw data. The draft of the manuscript was written by Yannik Rover and all authors commented on previous versions of the manuscript. All authors read and approved the final manuscript.

Funding
Open Access funding enabled and organized by Projekt DEAL. This work was financially supported by the German Federal Ministry of Education and Research; grant number 13FH173PX8. Furthermore, EU regional funding via the EFRE scheme of the State of Hesse is gratefully acknowledged.

Availability of data and materials
Data are available upon reasonable request to the authors.

Declarations

Competing interests
The authors declare that they have no known competing financial interests or personal relationships that could have influenced the work reported in this paper.

Received: 23 September 2022 Accepted: 23 January 2023
Published online: 01 February 2023

References

1. Holste K, et al (2020) Ion thrusters for electric propulsion: Scientific issues developing a niche technology into a game changer. Rev Sci Instrum 91:061101. https://doi.org/10.1063/5.0010134
2. International Electrotechnical Commission (2018) IEC standard 60050-161-01-07: International Electrotechnical Vocabulary: Electromagnetic compatibility: Basic concepts. https://www.electropedia.org/iev/iev.nsf/display?openform&ievref=161-01-07
3. Zhang H, et al (2021) Spacecraft Electromagnetic Compatibilities Technologies. Springer. ISBN 978-981-15-4781-2. https://doi.org/10.1007/978-981-15-4782-9
4. Rover Y, Volkmar C (2022) Verification of a radio-frequency generator mode in a full-wave 3D EM simulation. IEEE Aerospace Conference, Big Sky. 978-1-6654-3760-8/22/$31.00
5. Thueringer R, et al (2019) Test Facility for EMC-Characterization of Electric Thrusters in Operation using an evacuated Reverberation Chamber resp. an Anechoic Chamber with Vacuum Vessel and Honey Comb. IEPC-2019-A618 , University of Vienna, Austria
6. Beiting EJ, et al (2003) Electromagnetic Emissions to 60 GHz from a BPT-4000 EDM Hall Thruster. International Electric Propulsion Conference, IEPC-03-129, Toulouse

7. Baranov SV, et al (2017) Determination of Electromagnetic Emission from Electric Propulsion Thrusters under Ground Conditions. International Electric Propulsion Conference, IEPC-2017-167, Atlanta
8. Montag C, et al (2021) PETRUS 1J pulsed plasma thruster for the 3U GreenCube mission. 72nd International Astronautical Congress (IAC), Dubai
9. Kiefer F, et al (2022) Reverberation chamber for electromagnetic compatibility testing of electric thrusters. IEPC-2022-257, Massachusetts Institute of Technology, Cambridge
10. Hill DA (2009) Electromagnetic fields in cavities. Wiley-IEEE. ISBN 978-0-470-46590-5
11. Gustrau F (2015) Elektromagnetische Verträglichkeit. Hanser. ISBN 978-3-446-44301-3
12. Gustrau F (2019) Hochfrequenztechnik. Hanser, 3. ed.. ISBN 978-3-446-45950-2

Publisher's Note

Springer Nature remains neutral with regard to jurisdictional claims in published maps and institutional affiliations.

4 Diskussion und Fazit

Diese Forschungsarbeit beschäftigte sich mit EMV-Untersuchungen im Bereich der elektrischen Antriebstechnik für Raumfahrtanwendungen. Der Stand der Wissenschaft zeigte fehlende Erkenntnisse in dem Bereich der Vorhersagbarkeit des EMV-Verhaltens eines Systems auf. Die fehlenden Möglichkeiten, Triebwerkssysteme ganzheitlich und unter Nennbetrieb elektromagnetisch zu vermessen, waren eine weitere Problemstellung. Die durchgeführte Forschung und gewonnenen Erkenntnisse beantworten die Fragestellungen und haben für eine Erweiterung des Wissens und der Möglichkeiten in diesem Forschungsgebiet gesorgt. Die Beiträge dieser kumulativen Dissertation beschäftigen sich mit Simulationsmodellen eines Radiofrequenz-Generators sowie der Nachbildung des Ionenstrahls an einem Radiofrequenz-Ionentriebwerk. Weiterhin sind der Aufbau und die Inbetriebnahme einer halb-reflexionsfreien Absorberkammer mit angeschlossenem Vakuumtank in einem Beitrag beschrieben.

Weiterführende Arbeiten sollten sich mit der Ausweitung bzw. Zusammenführung der Simulationsmodelle beschäftigen. Zum einen ist die Erweiterung um ein Neutralisatormodell ratsam, um realitätsnahe Analysen zu erstellen.

Weiterhin lassen sich zusätzliche periphere Komponenten elektromagnetisch simulieren, wie die Hochspannungsnetzteile zum Betrieb des Gitterextraktionssystems. Bei der Zusammenführung aller Simulationskomponenten ist zum einen auf die Umsetzung der Simulationseinstellungen zu achten, da die einzelnen Modelle bereits rechenintensiv sind. Eine Möglichkeit wäre die Nutzung eines leistungsstarken Rechencluster bzw. die Zusammenführung der Emissionsspektren der einzelnen Komponenten als externe Störquelle in der Simulationsumgebung. Die gegenseitige Beeinflussung ist dadurch jedoch schwieriger nachzustellen. Eine weitere wichtige Komponente bei der Zusammenführung der Simulationen ist die Betrachtung des Kabelmanagements, da die Kabelauswahl sowie -führung erfahrungsgemäß einen entscheidenden Anteil am EMV-Verhalten des Gesamtsystems haben wird.

Zu den ausstehenden Forschungsarbeiten an der Absorberkammer selbst zählt die kontinuierliche Verbesserung der verwendeten Elemente, wie beispielsweise des Kunststoffzylinders oder des Wabenkamins. Die weitere Forschungsarbeit an der Absorberkammer umfasst die Vermessung aller Komponenten. Durch das schrittweise Hinzufügen bzw. Entfernen einzelner Komponenten ist ihr direkter Einfluss erkennbar. Weiterhin sind diverse Positionierungen von Komponenten und der Kabelführung zu erkunden. Um ebenfalls auf mögliche Missionen im Weltraum zu verweisen, ist der Betrieb mehrerer paralleler RIT zu erforschen, um die Interaktionen aus physikalischer und technischer Sicht zu verstehen. Dadurch ist die Ausarbeitung von Designregeln für sämtliche Triebwerkssystem-Zusammensetzungen möglich sowie die Zuarbeit bei einheitlichen Normen für die europäische Raumfahrt, organisiert durch die

europäische Kooperation für Raumfahrtnormung der Europäischen Weltraumorganisation ESA.

Zuletzt sollte das Ziel die Vereinigung von Messungen und Simulationsmodell für ähnliche Betriebsparameter sein. Dadurch wird eine endgültige Verifizierung des Simulationsmodells erreicht und für die Vorentwicklung, sowohl für Triebwerke wie auch Elektronik, verwendbar.

Literatur

[Bar17] Baranov, S. V., et al.: „Determination of Electromagnetic Emission from Electric Propulsion Thrusters under Ground Conditions“, IEPC-2017-167, 2017 International Electric Propulsion Conference, Atlanta, US (2017), http://electricrocket.org/IEPC/IEPC_2017_167.pdf

[Bat17] Baruth, T.: „Analysis on the electromagnetic compatibility of radio-frequency ion thrusters using a RIT4“, University of Giessen, Giessen, Germany (2017), http://geb.uni-giessen.de/geb/volltexte/2017/12495/

[Bei03] Beiting, E.J., et al.: „Electromagnetic Emissions to 60 GHz from a BPT-4000 EDM Hall Thruster“, IEPC-03-129, 2003 International Electric Propulsion Conference, Toulouse, France (2003), http://electricrocket.org/IEPC/0129-0303iepc-full.pdf

[Cha11] Chabert, P., Braithwaite, N.: „Physics of Radio-Frequency Plasmas“, University Press, Cambridge (2011), ISBN 978-0-521-76300-4

[Gus15] Gustrau, F., Kellerbauer, H.: „Elektromagnetische Verträglichkeit“, Hanser (2015), ISBN 978-3-446-44301-3

[Hol20] Holste, K., et al.: „Ion thrusters for electric propulsion: Scientific issues developing a niche technology into a game changer“, Rev. Sci. Instrum. 91, 061101 (2020), https://doi.org/10.1063/5.0010134

[Int18] International Electrotechnical Commission, „IEC standard 60050-161-01-07: International Electrotechnical Vocabulary: Electromagnetic compatibility: Basic concepts“ (2018)

[Jun19] Junker, J. E., Probst, U., Klar, P. J.: „Development of a full bridge series resonant radio-frequency generator for optimized RIT operation“, IEPC-2019-474, 2019 International Electric Propulsion Conference, Vienna, Austria (2019), https://electricrocket.org/2019/474.pdf

[Lan20] Lan, C., Kaganovich, I. D.: „Neutralization of ion beam by electron injection: Accumulation of cold electrons“, Phys. Plasmas 27, 043108 (2020), https://doi.org/10.1063/1.5128521

[Men16] Meniconi, G., et al.: „Electromagnetic Emissions from the Fakel SPT-100 Thruster Measured at the new Aerospazio EMI Test Facility“, F-31402, 2016 Space Propulsion, Roma, Italy (2016)

[Mon00] Montrose, M. I.: „Printed Circuit Board Design Techniques for EMC Compliance: A Handbook for Designers“, Wiley (2000), ISBN 0-7803-5376-5

[Mue92] Müller, H., Kukies, R., Bassner, H.: „EMC Tests on the RITA Ion Propulsion Assembly for the ARTEMIS Satellite“, AIAA 92-3208, 28th Joint Propulsion Conference and Exhibit, Nashville, US (1992), https://doi.org/10.2514/6.1992-3208

[Ott11] Ott, H. W.: „Electromagnetic Compatibility Engineering“, Wiley (2011), ISBN 978-0470189306

[Per19] Perez, R. J.: „Handbook of Aerospace Electromagnetic Compatibility“, Wiley (2019), ISBN 978-111-89-1051-1

[Rov22] Rover, Y., Volkmar, C.: „Verification of a radio-frequency generator model in a full-wave 3D EM simulation“, 2022 IEEE Aerospace Conference (AERO), Big Sky, MT, USA (2022), pp. 1-10, https://doi.org/10.1109/AERO53065.2022.9843355

[Rov23] Rover, Y., et al.: „Modeling the influence of an electric thruster's ion beam on its global EMC“, Front. Space Technol. 4:1287474 (2023), https://doi.org/10.3389/frspt.2023.1287474

[Roy23] Rover, Y., et al.: „Semi-anechoic chamber for electromagnetic compatibility tests of electric propulsion thrusters“, J Electr Propuls 2, 3 (2023), https://doi.org/10.1007/s44205-023-00039-w

[Thu19] Thüringer R., et al.: „Test Facility for EMC-Characterization of Electric Thrusters in Operation using an evacuated Reverberation Chamber resp. an Anechoic Chamber with Vacuum Vessel and Honey Comb“, IEPC-2019-A618, 2019 International Electric Propulsion Conference, Vienna, Austria (2019), https://electricrocket.org/2019/618.pdf

[Usu13] Usui, H., Hashimoto, A., Miyake, Y.: „Electron behavior in ion beam neutralization in electric propulsion: full particle-in-cell simulation“, J. Phys.: Conf. Ser. 454 012017 (2013), https://doi.org/10.1088/1742-6596/454/1/012017

[Zha21] Zhang, H., et al.: „Spacecraft Electromagnetic Compatibilities Technologies“, Springer (2021), ISBN 978-981-15-4781-2, https://doi.org/10.1007/978-981-15-4782-9